2014年2月 碩士學位論文
Characteristics of CIGS Thin Films Fabricated by Using Post-Annealing Processes after Sputtering
吳 成 夏

2014年 2月

碩士學位 論文

Characteristics of CIGS Thin Films Fabricated by Using Post-Annealing Processes after Sputtering

朝鮮大學校 大學院

電氣工學科

吳 成 夏

Characteristics of CIGS Thin Films Fabricated by Using Post-Annealing Processes after Sputtering

스퍼터링 및 후속 열처리 공정으로 제조한
CIGS 박막 특성

2014年 2月 25日

朝鮮大學校 大學院

電氣工學科

吳 成 夏

Characteristics of CIGS Thin Films Fabricated by Using Post-Annealing Processes after Sputtering

指導敎授　李 愚 宣 · 金 南 勳

이 論文을 工學碩士學位 申請論文으로 提出함.

2013年 10月

朝鮮大學校 大學院

電氣工學科

吳　成　夏

吳成夏의 碩士學位論文을 認准함

委 員 長　朝鮮大學校 敎授 曺 錦 培 印

委　　員　朝鮮大學校 敎授 崔 孝 祥 印

委　　員　朝鮮大學校 敎授 李 愚 宣 印

2013年 11月

朝鮮大學校 大學院

Contents

List of Tables

List of Figures

ABSTRACT

스퍼터링 및 후속 열처리 공정으로 제조한 CIGS 박막 특성

Oh, Seongha

Advisor : Prof. Lee, Woo-Sun, Ph D.

Prof. Kim, Nam-Hoon, Ph D.

Department of Electrical Engineering

Graduate School of Chosun University

최근 칼코파이라이트 격자구조인 다결정 CIGS 박막이 태양전지 산업에서 흡수층으로서 커다란 관심을 받고 있다. 그 이유는 이종접합 구조를 갖는 CIGS 태양전지가 기존의 다결정 실리콘 태양전지의 최고 효율과 대등한 20.4%의 변환효율을 달성하였기 때문이다. 뿐만 아니라 Ga/(In+Ga)의 화학적 조성 비율에 의해서 밴드갭 에너지(1.04 ~ 1.68eV)를 조정할 수 있다는 특성이 CIGS 박막에 관심을 쏟게 만드는 원인이 되고 있다. 종래의 CIGS 제조 공정에는 동시증발법과 후속 셀렌화 공정이 널리 통용되고 있지만 공정의 복합성과 느린 증착속도 및 낮은 재현성과 고비용이라는 단점을 지니고 있다. 이러한 단점을 보완하기 위하여 본 논문에서는 $CuSe_2$ 합금 타겟과 In 및 Ga 타겟을 사용한 스퍼터링 공정을 통해 셀레늄과 황화 가스 분위기를 배제한 방법을 제안하였다. 게다가 다양한 어닐링 공정으로는 로(Furnace)열처리, 급속열처리(RTA), 레이저어닐링등을 이용하여 박막의 특성을 개선하는 연구를 진행하였다. 먼저 RF 스퍼터링 방법으로 증착한 CIGS 박막에 전기로 열처리와 급속열처리를 수행한 시료들의 특성을 비교 분석하였다. 이후 다층 구조($CuSe_2$/Ga/In/$CuSe_2$)로 스퍼터링 증착한 CIGS 박막의 Ga/(In+Ga)의 두께비의 조절을 통해 Ga 및 In 성분비 제어 가능성 타진과 최

적 공정조건으로 제조한 CIGS 박막의 특성을 분석하였다. 마지막으로 RF 스퍼터링을 통해 CIGS 박막을 증착한 후, Nd:YAG(532nm) 레이저의 파워를 달리하여 레이저어닐링을 수행한 박막의 특성에 대하여 비교 연구하였다. 이와 같은 모든 실험에서 CIGS 박막의 결정과 구조적 특성을 분석하기 위하여 X-ray diffraction(XRD)를 사용하였고, 전기적·광학적 특성을 분석하기 위해 UV-Visible spectrophotometer과 Hall effect measurement system을 사용하였다. 실험결과 400℃에서 RTA를 수행한 박막에서 전기로에서 열처리한 박막에 비해 전기적·광학적 특성이 더욱 우수하였다. Ga/(In+Ga)의 두께비를 조절 비교한 실험에서는 분석을 통해 비율이 0.5에서 0.2로 감소할수록 저항이 $3.72\times10^{2}\Omega$-cm에서 $6.15\times10^{-3}\Omega$-cm으로 감소하였고, 밴드갭 에너지 역시도 1.88eV에서 1.73eV으로 한다는 결과를 확보할 수 있었다. 뿐만 아니라, 레이저어닐링을 사용해서 CIGS에 해당하는 칼코파이라이트 상을 형성할 수 있음을 확인하였고, 3.2 watt로 레이저 어닐링을 수행하였을 때 최적의 특성을 확보하였다. 최종적으로 본 논문을 통해 우수한 품질을 가지는 대면적의 대량 생산이 가능한 CIGS 박막을 스퍼터링 방법으로 제작이 가능하였으며, 셀렌화/황화 공정의 배제로 저가의 비오염/저위험성 공정이 가능한 새로운 방법을 제시하였다. 기존 전기로 열처리 공정에 급속열처리 공정을 최적화 하였으며, 새롭게 레이저어닐링 공정을 제안하여 우수한 특성의 CIGS 박막의 제조가 가능해짐에 따라 높은 효율을 갖는 고품질의 CIGS 박막 태양전지를 얻을 수 있을 것으로 기대된다.

Ⅰ. Introduction

In recent years, the solar cell industry has grown rapidly due to the abrupt increase in oil prices and concern about the environment. This has caused a marked increase in the market demand for solar cells, a key technology in this industry. Considerable attention has been paid to thin film solar cells including polycrystalline copper indium gallium diselenide ($CuIn_{1-x}Ga_xSe_2$, CIGS) thin films with a chalcopyrite lattice structure as an absorber layer owing to its suitable optical absorption (> 10^5 cm^{-1}), long-term electro-thermal stability, high tolerance to defects, no toxic or hazardous pollutants, such as arsenic and cadmium, and a tunable bandgap (1.04 - 1.68 eV) by adjusting the chemical composition ratio of Ga /(In + Ga) [1,2]. The highest conversion efficiency exceeding 20.4% has been achieved in heterostructured CIGS solar cells [3], which is approaching the highest efficiency of conventional polycrystalline silicon solar cells [4,5].

A co-evaporation and post-selenization process is widely employed for achieving high conversion efficiency but this conventional method has several drawbacks impeding industrial production, such as process complexity, expensive equipment, slow deposition rate and poor reproducibility [6]. Against the conventional manufacturing processes, the selenization of sputtered Cu-In-Ga precursors using H_2Se vapor was proposed as a suitable method for preparing CIGS thin films at low cost [7]. On the other hand, critical problems in the selenization process still remains, such as highly toxic H_2Se,slow reaction rate and poor adhesion with backcontact [1]. Therefore, a non-selenization process is needed to prepare CIGS thin films.

Few studies have been performed: AVANCIS GmbH and Co. KG formed an elemental precursor film by DC-magnetron sputtering of Cu-In-Ga and the thermal evaporation of Se followed by rapid thermal annealing (RTA) in a sulfur containing ambient [8,9]. Jheng *et al.* prepared CIGS thin films by co-sputtering with Cu-Ga alloy and In-Se alloy targets before a two-step annealing process

without an additional selenium source under vacuum [1]. Meanwhile, laser annealing process has been performed restrictively in silicon solar cell applications for crystallization and grain growth to improve the efficiency [10,11]. The laser annealing process for thin film solar cells has several advantages including localized high thermal treatments, excellent annealing selectivity to the underlayers or substrate, short process duration, precise control of the heating time and zone, and superior ramp-up rate [12-15].

In this thesis, chalcopyrite CIGS thin films were prepared by using RF magnetron sputtering with In, Ga, and $CuSe_2$ alloy targets without any selenization process in annealing process. This proposed method has some advantages including simplicity, large-area manufacturing for mass production, and easy adjustment of the chemical composition of Ga / (In + Ga) ratio. The laser annealing effects were also investigated on the structural, chemical, electrical and optical properties of the $Cu(In,Ga)Se_2$ as a function of laser power.

Ⅱ. Theoretical Background

A. Solar cell

1. Principles of Solar Cell

A solar cell is an electrical device that converts the energy of light directly into electricity by the photovoltaic effect. It is a form of photoelectric cell which can generate and support an electric current when exposed to light without being attached to any external voltage source. Photovoltaic energy conversion in solar cells consists of two essential steps. First, absorption of light generates an electron-hole pairs. The electron and hole are separated by the structure of the device, thus generating electric power with electrons to the negative terminal and holes to the positive termainal. This process is illustrated in Figure 1.

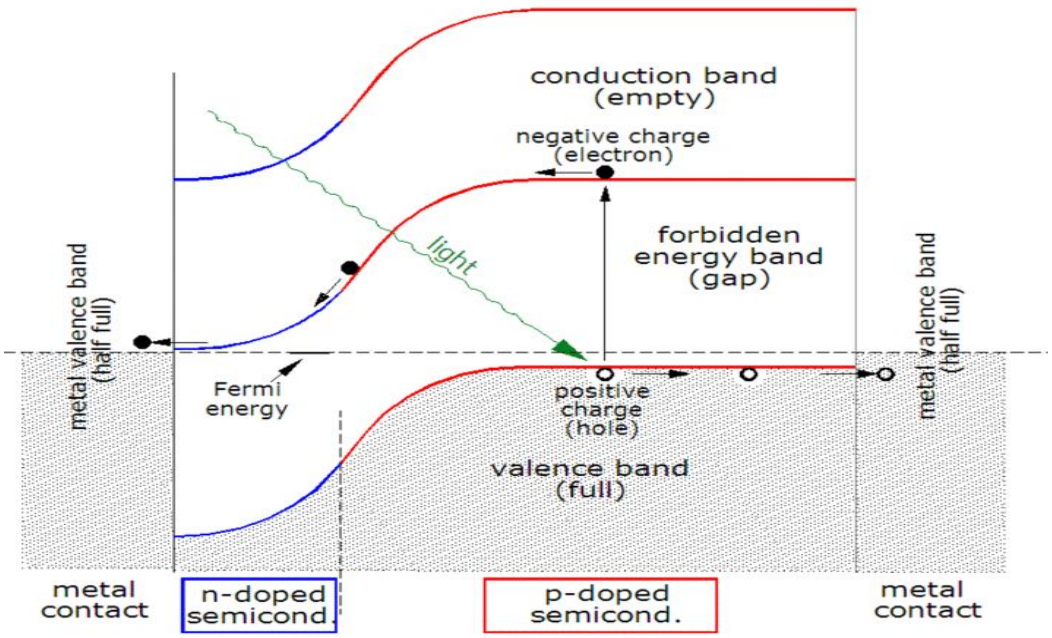

Fig. 1 Principle of p-n junction solar cell

The solar cell consists of a junction formed between n-type and p-type semiconductors, either of the same material (homojunction) or different materials (heterojunction). The bandstructure of the two differently doped sides with respect to their Fermi levels can be seen in Figure 1. When the two halves are brought together, the Fermi levels on either side are forced in to coincidence, causing the valence and conduction bands to bend. These bent bands represent a built-in electric field over what is referred to as the depletion region. When a photon, with an energy greater than the band gap of the semiconductor, passes through the solar cell, it may be absorbed by the material. This absorption takes the form of a band-to-band electronic transition, so an electon/hole pair is produced. If these carriers can diffuse to the depletion region before they recombine, then they are separated by the electric field, causing one quantum of charge to flow through an external load. Therefore, the p-n junction separates the carriers with opposite charge, and transforms the generation current between the bands into an electric current across the p-n junction.

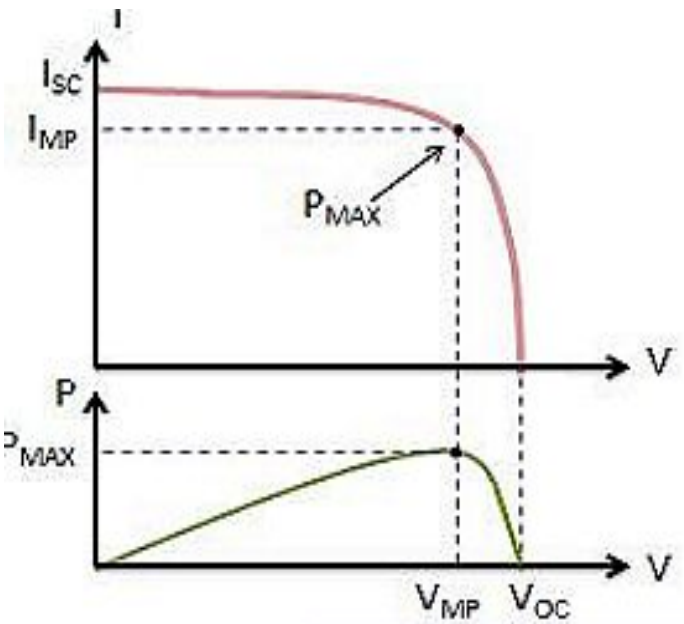

Fig. 2 I-V curve for maximum power

A more detailed consideration makes it possible to draw an equivalent circuit of a solar cell in terms of a current generator and a diode. This equivalent circuit has a current-voltage relationship. In solar cell applications this characteristic is usually drawn inverted about the voltage axis, as shown Figure 2. The cell generates no power in short-circuit when current I_{sc} is produced or open-circuit when cell generates voltage V_{oc}. The cell delivers maximum power P_{max} when operating at a point on the characteristic where the product I-V is maximum.

2. Classification

Generally solar cell is distinguished in three steps by the energy conversion efficiency and manufacturing cost.

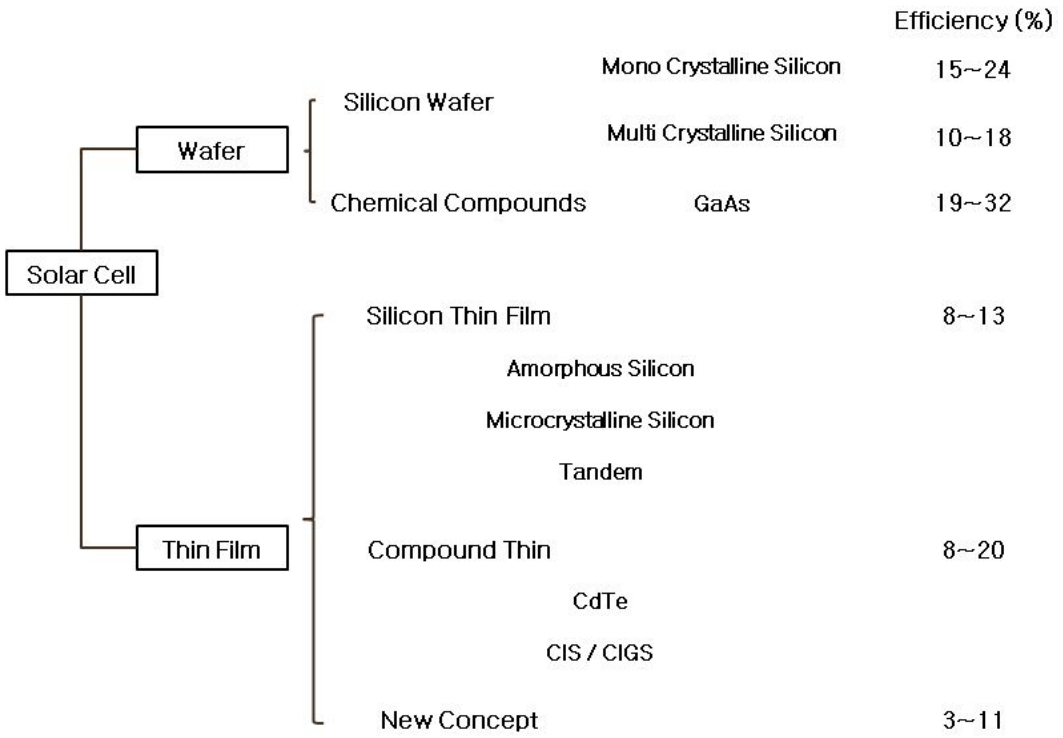

Fig. 3 Classification of the solar cells

First generation solar cells are generally made using a crystalline silicon wafer. The typical silicon solar sell is composed of a thin wafer consisting of an ultra-thin layer of phosphorus (P)-doped silicon on top of a thicker layer of boron (B)-doped silicon. The efficiency of the first generation crystalline solar cell module is 10～18%.

Second generation cells are based on the thin film solar cells. Amorphous silicon cells, cadmium telluride (CdTe), and copper indium gallium diselenide (CIGS) alloy cells are included. The great advantage of these are lower manufacturing costs, reduced mass, and allowance of fitting panels on light or flexible materials. However, the efficiencies of these are lower than silicon wafer solar cells up to recently.

Third generation solar cells are using the materials of nano semiconductor and organic semiconductor. These do not rely on a traditional p-n junction to separate photo-generated charge carriers. Third generation solar cells are possible to fabricate simply with the low cost and can be used for many real applications. However, the efficiencies of these are under 5%, moreover, the reliability of fabricated modules is insufficient.

B. CIGS Thin Film Solar Cell

1. Structure of CIGS Thin Film Sloar Cell

The structure of CIGS thin film solar cells are composed by the formation of multi-layer thin films, as shown in Figure 4. molybdenum (Mo) and zinc oxide (ZnO) thin films are used in the back and the front electrode, the CIGS thin film is used as a light absorption layer. Between, the optical absorption layer and ZnO thin films, cadmium sulfide (CdS) thin film as a buffer layer is formed. The general characteristics of each unit of the films are as follows;

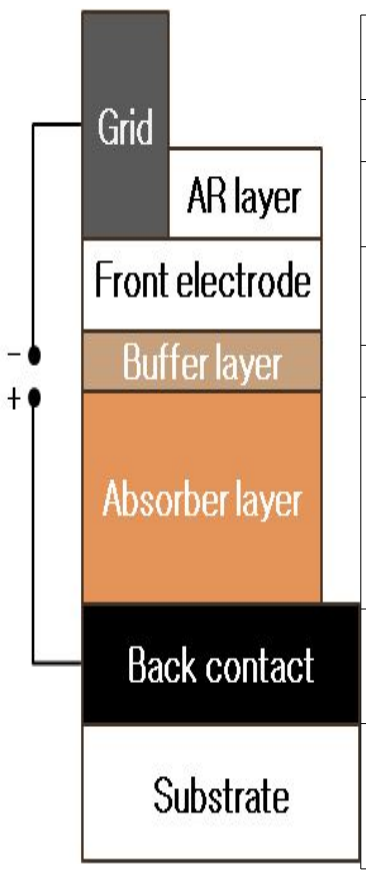

Thickness, Materials	Process
3 μm, Al / 50nm, Ni	E-beam evaporation
MgF_2	E-beam evaporation
500 nm, n-ZnO / 50 nm, i-ZnO	RF sputtering
50nm, CdS	CBD
0.5~3 μm, $Cu(In,Ga)Se_2$	RF sputtering
1 μm, Mo	DC sputtering
2-3 mm, Glass	Cleaning

Fig. 4 Structure of CIGS solar cells

a. Substrate

Soda-lime glass (SLG) has been used as the typical substrate material for CIGS solar cells because it is cheap and has many advantages for high efficiency solar cells. The main beneficial effect of SLG on the cell performance is the natrium (Na) diffusion into CIGS absorber. Because the incorporated Na enhanced the open circuit voltage(V_{OC}) and fill factor (FF) [16,17]. Na doping is indispensible for high-efficiency CIGS solar cell. Usage of SLG substrate, therefore, becomes a cost-reducing factor for solar cell fabrication since additional Na doping process is needless. The smooth surface can be also the advantage of SLG.

b. Back Contact

Nowadays, DC-sputtered Mo thin films have been used as the back contact material for CIGS solar cells. Mo thin films are usually deposited on the substrate using a DC-sputtering. The Mo layers with a thickness of around 1 μm deposited are generally used for the CIGS solar cells. With the excellent properties of low contact resistance to the CIGS, relative stability at the processing temperatures (400~600°C). DC-sputter method is preferred to the RF-sputtering method for Mo. The properties of Mo layer are affected by the deposition pressure.

c. Buffer Layer

CIGS solar cells with a buffer layer have superior characteristics compared to those without. Heterojunction solar cells inevitably have a large lattice mismatch at the interface, resulting in enhanced interface defect states. The introduction of buffer layers, in particular CdS, between CIGS and ZnO can improve the junction property: lower interface recombination (decreased leakage), protection

of the absorber surface against damage from ZnO sputtering, surface etching in the chemical bath used to deposit the CdS and the in-diffusion of Cd into the absorber [18-20].

d. Front Electrode

ZnO thin films deposited by RF sputtering with a ZnO target or reactive sputtering using Zn metal and metal organic material deposited by a CVD method currently being used. CIGS and ZnO thin film can achieve p-n junction, but it has the interfacial defects because of the large lattice mismatch [21,22]. The ZnO thin film has about 3.3 eV energy band gap and appromimately 80% or higher light transmittance. In addition, a low-resistance n-type ZnO thin film on top of a very thin layer of CdS at the interface of 50 nm is formed by an increse in diode shunt components. The bilayer deposition to 500nm has been reported to be able to process can improve the solar cell characteristics.

e. Grid

In order to prevent the resistive losses caused by the formation of alumina (Al_2O_3) between grid and aluminum zinc oxide (AZO) [23], the insertion of a thin nickel (Ni) layer is general: bilayer Ni/Al grid structure. Ni (50 nm) / Al (850 nm) grids were deposited on the AZO surface of samples using a e-beam evaporator. The grid patterns were translated by using a shadow mask made of stainless-steel.

2. Characteristics of CIGS Thin Film

Recently, the 20% efficiency limit for CIGS solar cells was surpassed, and a champion cell efficiency of 20.4% was recorded by EMPA in Switzerland [24]. The compounds of CuInSe2 and Cu(In,Ga)Se2 with their chalcopyrite structures are among the most promising materials used in thin film solar cells, as shown Figure 5.

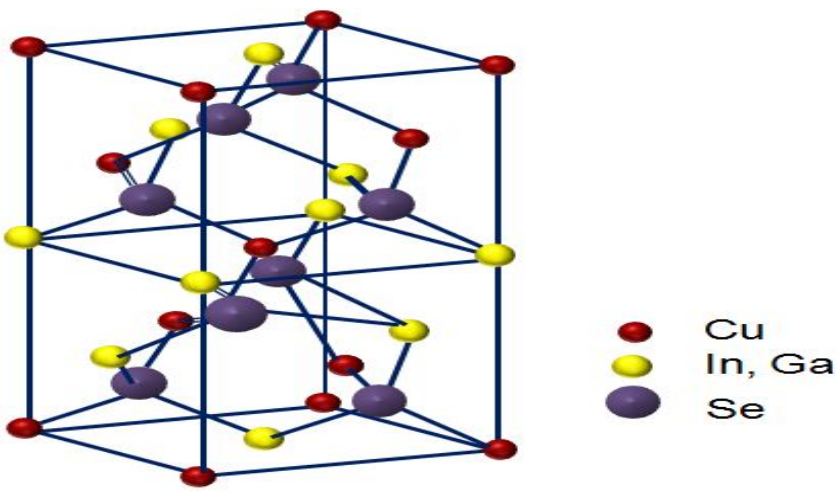

Fig. 5 CIGS chalcopyrite structure

The main advantages of CIGS-based solar cells are the high conversion efficiency and low cost of materials. The CIGS absorber is direct band gap material with band gap tunable by adjusting the ratio of In to Ga, to maximize absorption of the solar spectrum. Its band gap can be varied from 1.04eV to 1.68eV.

Thin-film CIGS material also has a higher absorption coefficient than any other thin film, which allows almost 99% of the incoming light to be absorbed with the first micron of the material according to the solar spectrum.

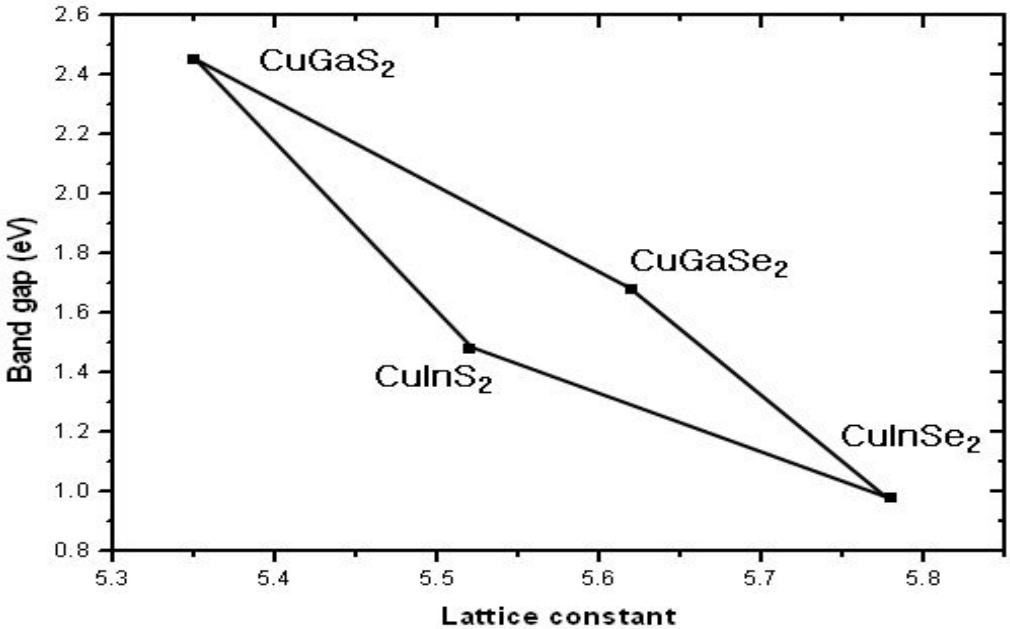

Fig. 6 Bandgap versus lattice constant diagram of CIGS solar cell

3. Technolngy Trend of CIGS Thin Film

CIGS solar cells have drawn attention as low-cost, high-efficiency solar cells to replace existing expensive c-Si solar cells and improve economic feasibility of photovoltaics. The market is expected to continue to post over 20% growth in the future. The plus factors driving the growth can be predicted from the cases in other thin-film solar cells. Dye-selenized solar cell (DSSC) and organic photovoltaics (OPV) manufacturers have experienced delays in commercialization of their products. Although DSSCs and OPVs are inferior to CIGS solar cells in terms of performance, they can meet the demand from niche markets (mobile chargers, etc.) due to such advantages as transparency and flexibility. Nevertheless, commercialization of them has been delayed due to safety and reliability issues, which would serve as an opportunity for flexible CIGS solar cells.

Fig. 7 CIGS thin-film solar cell manufacturing capacity and production forecast

Additionally, as the current oversupply of c-Si solar cells is relieved and the price gap between with CIGS solar cells would be narrowed, CIGS solar cells would be able to secure their price competitiveness again. Based on the above analysis, the GIGS thin-film solar cell production is expected to exceed 3 GW in 2015, reaching $3.2 billion.

C. Principles of Sputtering

Sputtering is a process whereby atoms are ejected from a solid target material due to bombardment to the target by energetic particles. It only happens when the kinetic energy of the incoming particles is much higher than conventional thermal energies. This process can lead, during prolonged ion or plasma bombardment of a material, to significant erosion of materials, and can thus be harmful. On the other hand, it is commonly utilized for thin-film deposition. Sputter deposition is a method of depositing thin films by sputtering that involves eroding material from a target source onto a substrate, as shown in Figure 7.

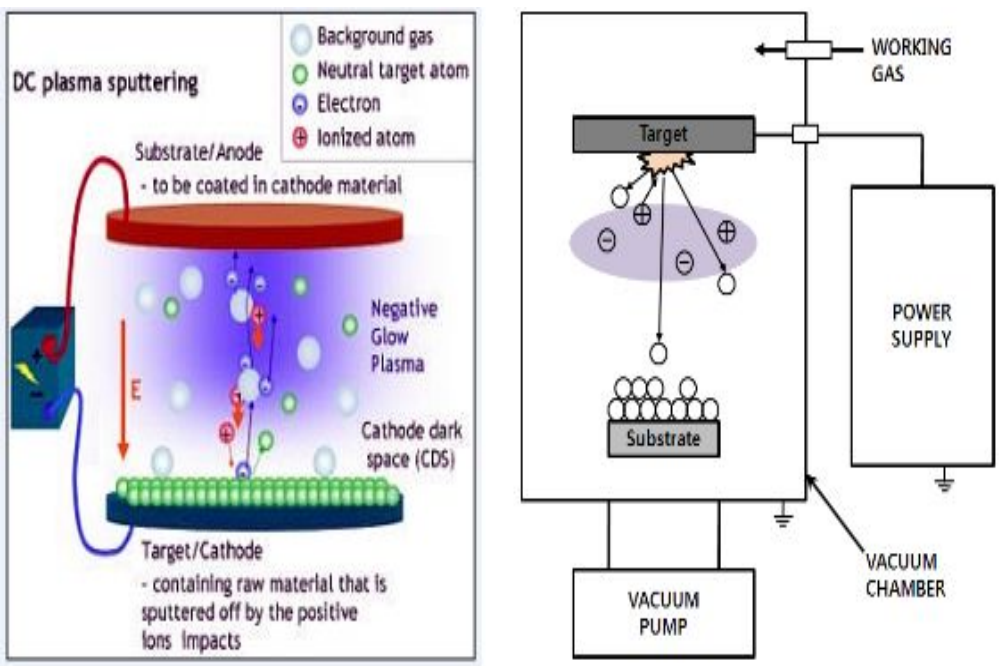

Fig.8 Basic schematic diagram of sputter equipment

In operation, the source of coating material, themed the targret, is mounted the opposite the substrates in a vacuum chamber which is then evacuated to a base pressure of typical range from 10^{-6} to 10^{-10} Torr, depending upon the process. The most common method of proving the ion bombardment necessary for sputtering is to backfill the evacuated chamber, using a continuous flow of a gas such as argon (Ar), to a pressure of from 1 to 100 mTorr, and establish a glow discharge. The most noticeable characteristic of the sputtering process is its universality. Since the coating material is passed into the vapor phase by a physical momentum-exchange process, rather than a chemical or thermal process, virtual any material is a coating candidate. DC discharge methods are generally used for sputtering metal, while a RF potential must be applied to the target when sputtering nonconducting materials.

Fig.9 Sputter equipment (Vacuum Science Co.)

D. Principles of Annealing

1. Furnace Annealling

Furnace annealing is a process used in materials processing which consist of heating wafers in order to affect their structural and electrical properties. Heat treatments are designed for different effects. Wafers can be heated in order to activate dopants, change film to film or film to wafer substrate interfaces, densify deposited films, change states of grown films, repair damage from implants, move dopants or drive dopants from one film into another or from a film into the wafer substrate. Furnace anneals may be integrated into other furnace processing steps, such as oxidations.

2. Rapid Thermal Annealing (RTA)

Rapid thermal annealing (RTA) is a subset of rapid thermal processing. It is a process used in materials processing which consists of heating a single wafer at a time in order to affect its structural and electrical properties. Unique heat treatments are also designed for different effects. Wafers can be heated in order to activate dopants, change film-to-film or film-to-wafer substrate interfaces, densify deposited films, change states of grown films, repair damage from ion implantation, move dopants or drive dopants from one film into another or from a film into the wafer substrate. Rapid thermal anneals are performed by equipment using lamp based heating, a hot chuck, or a hot plate that a wafer is brought near. Unlike furnace anneals they are short in duration, processing each wafer in several minutes. To achieve short time annealing time trade off is made in temperature and process uniformity, temperature measurement and control and wafer stress as well as throughput.

Fig.10 Rapid thermal annealing equipment
(Modular Process Technology Co., RTP-600S)

3. Laser Annealing

The aggressive scaling down of gate dimension of ultra large scale integrated (ULSI) devices for the improvements of performance and speed has aggravated the short channel effects (SCE), which cause excessive leakage to the devices [25]. As a result, the need for ultra-shallow junctions becomes more critical to suppress the SCE [26]. Laser annealing has been identified as one of the promising candidates for post-implantation annealing process for the fabrication of abrupt, highly activated and ultra-shallow junctions necessary for nano-scale semiconductor devices [27-29]. Laser annealing of semiconductors has some advantages, such as localized high temperatures with excellent annealing sselectivity to the underlayers or substrate for a short process duration and precise control of the heating time and zone. Laser annealing has a superior

ramp-up rate (up to 108 times higher) compared to the rapid thermal process (RTP) and can provide a very selective annealing process. The scaling-down of devices requires precise control of the annealing process in order to realize negligible diffusion and very low sheet resistance [16].

E. Analysis of CIGS Thin Film

1. Structural Characteristics of Thin Film by XRD

X-ray diffraction (XRD) is an analytical technique looking at X-ray scattering from crystalline materials. Each material produces a unique X-ray "fingerprint" of X-ray intensity versus scattering angle that is characteristic of its crystalline atomic structure. Qualitative analysis is possible by comparing the XRD pattern of an unknown material to a library of the known patterns. Approximately 95% of all solid materials can be described as crystalline. When X-rays interact with a crystalline substance (phase), one gets a diffraction pattern. The X-ray diffraction pattern of a pure substance is, therefore, like a fingerprint of the substance. The powder diffraction method is thus ideally suited for characterization and identification of polycrystalline phases.

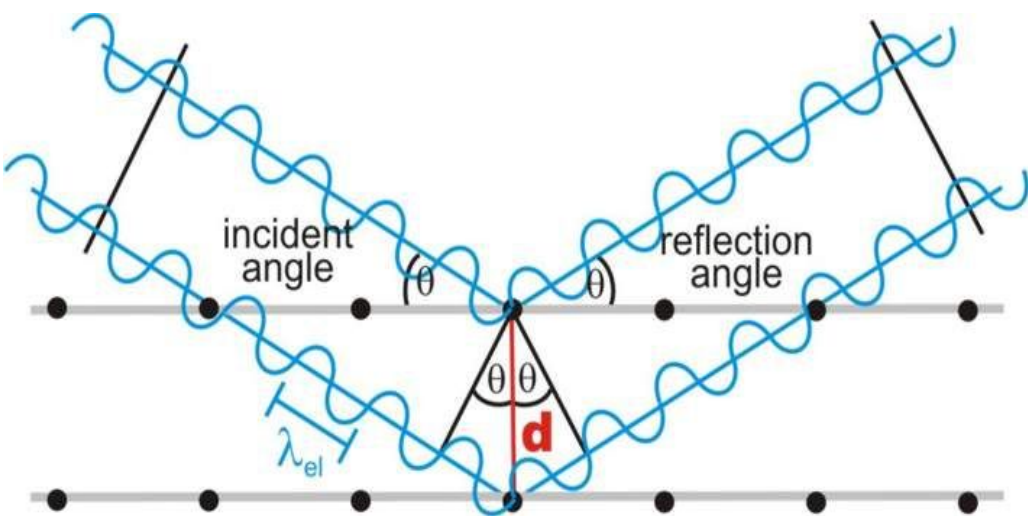

Fig.11 Diagram of Bragg's Law in X-ray diffraction

The two parallel incident rays 1 and 2 make an angle (θ) with these planes. A reflected beam of maximum intensity will result if the waves represented by 1'and 2'are in phase. The difference in path length between 1 to 1' and 2 to 2' must then be an integral number of wavelengths (λ). This relationship can be expressed mathematically in Bragg's law.

$$2d \sin \theta = n \lambda$$

The process of reflection is described here in terms of incident and reflected (or diffracted) rays, each making an angle θ with a fixed crystal plane. Reflections occurs from planes set at angle θ with respect to the incident beam and generates a reflected beam at an angle 2θ from the incident beam. The possible d-spacing defined by the indices h, k, l are determined by the shape of the unit cell. Rewriting Bragg's law we get :

$$\sin \theta = \lambda/2d$$

The possible 2θ values can be known are determined by the unit cell dimensions where reflections. However, the intensities of the reflections are determined by the distribution of the electrons in the unit cell. The highest electron density are found around atoms. Therefore, the intensities depend on what kind of atoms and where located in the unit cell. Planes going through areas with high electron density will reflect strongly, planes with low electron density will give weak intensities.

Fig. 12 XRD equipment (Philips X'pert-PRO-MRD XRD)

2. Electrical Characteristics Analysis of Thin Film by Hall Effect Measurement System

Consider a conducting slab, as shown in Figure 11, with length L in the x direction, width W in the y direction and thickness T in the z direction.

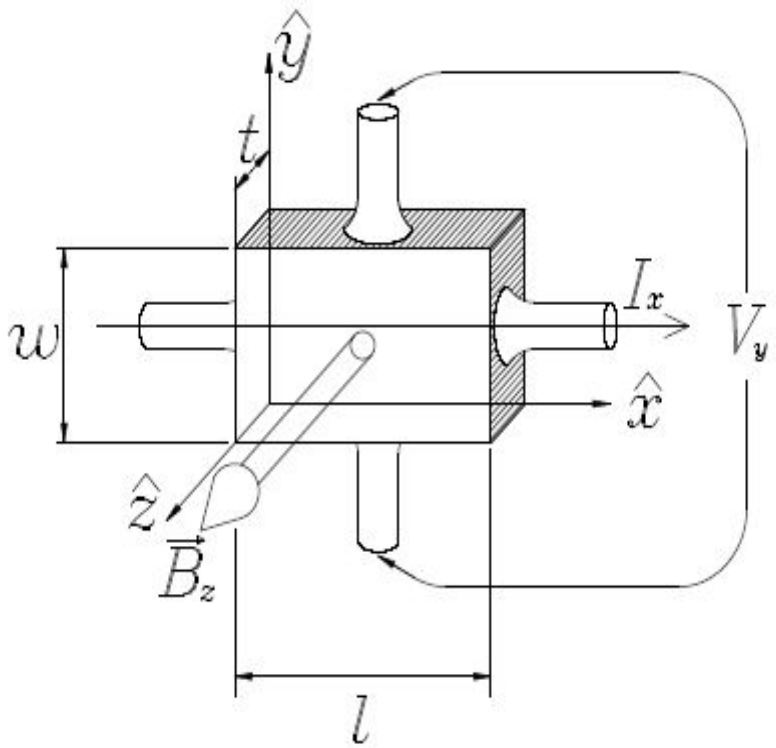

Fig. 13 Geometry of fields and sample in Hall effect experiment

Assume the conductor to have charge carrier of charge q, charge carrier number density n, and charge carrier drift velocity v_x when a current flows in the positive x direction. The drift velocity is an average velocity of the charge carriers over the volume of the conductor; each charge carrier may move in a seemingly random way within the conductor, but under the influence of applied fields there will be a net transport of carriers along the length of the conductor. The current I_x is the current density J_x times the cross-sectional area of the

conductor WT. The current density J_x is the charge density nq times the drift velocity v_x. In other words

$$I_x = J_x WT = nqv_x WT$$

The current I_x is caused by the application of an electric field along the length of the conductor E_x. In the case where the current is directly proportional to the eld, the material obeys Ohm's law, which may be written :

$$J_x = \sigma E_x$$

,where σ is the conductivity of the material in the conductor.

Fig. 14 Hall Effect measurement system equipment (Accent Optical Technologies. HL5500PC)

3. Optical Characteristic of Thin Film by UV-visible Spectro-photometer

A diagram of the components of a typical UV-visible spectrometer are shown in Figure 13. The functioning of this instrument is relatively straightforward. A beam of light from a visible and/or UV light source is separated into its component wavelengths by a prism or diffraction grating. Each monochromatic beam in turn is split into two equal intensity beams by a half-mirrored device. One beam, the sample beam, passes through a small transparent container containing a solution of the compound being studied in a transparent solvent. The other beam, the reference, passes through an identical cuvette containing only the solvent. The intensities of these light beams are then measured by electronic detectors and compared.

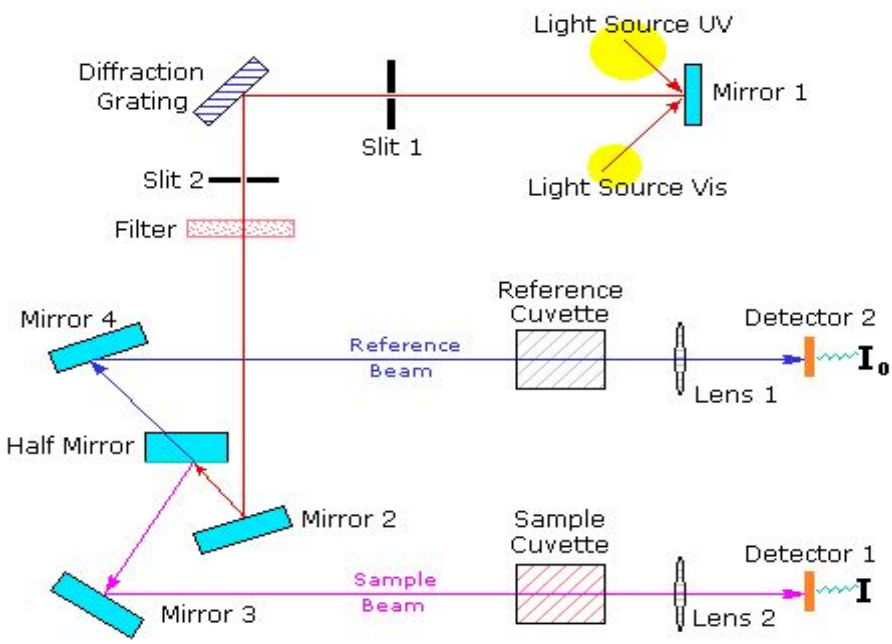

Fig. 15 Diagram of UV-visible spectroscopy

The intensity of the reference beam, which should have suffered little or no light absorption, is defined as I_0. The intensity of the sample beam is defined as I. Over a short period of time, the spectrometer automatically scans all the component wavelengths in the manner described. The UV-region scanned is normally from 200 to 400 nm, and the visible portion is from 400 to 800 nm. If the sample compound does not absorb light of a given wavelength, $I = I_0$. However, if the sample compound absorbs light then I is less than I_0, and this difference may be plotted on a graph versus wavelength, as shown on the right. Absorption may be presented as transmittance ($T = I/I_0$) or absorbance ($A = \log I_0/I$). If no absorption has occurred, T = 1.0 and A = 0. Most spectrometers display absorbance on the vertical axis, and the commonly observed range is from 0 (100% transmittance) to 2 (1% transmittance). The wavelength of maximum absorbance is a characteristic value, designated as λmax.

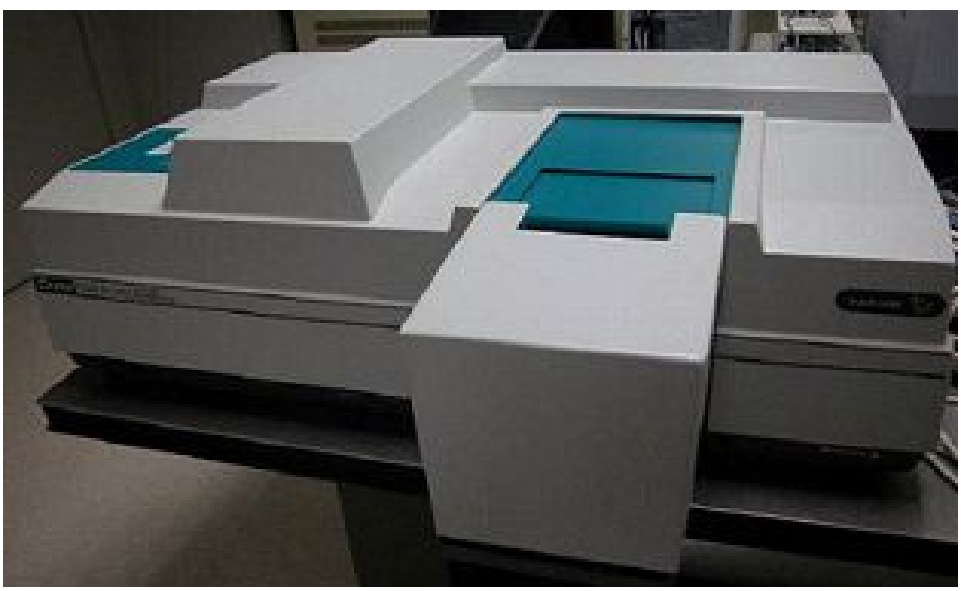

Fig. 16 UV-visible Spectrophotometer equipment
(Varian Techtron. Cary 500 scan)

Ⅲ. Non-Selenization Method using Sputtering Deposition with a $CuSe_2$ Target for CIGS Thin Film

Significant progress in the heterostructured CIGS solar cell has been achieved the highest conversion efficiency exceeding 20.4%, which is the value closing in upon the highest efficiency of the traditional polycrystalline silicon solar cell [3]. Non-selenization process is thereby required to be developed for preparing CIGS thin film, but very few investigations were performed. This work demonstrates a chalcopyrite CIGS thin film without any selenization process by using RF magnetron sputtering with In, Ga and $CuSe_2$ alloy targets. This proposed method has some advantages including simplicity, large-area manufacturing for mass production, and easiness for adjusting chemical composition of Ga / (In + Ga) ratio.

A. Experimental Details

The RF magnetron sputtering (Vacuum Science Co.) method was employed for the preparation of 250 nm-thick $CuSe_2$ thin films on 2×2 cm ITO/Corning glass substrates with a commercial $CuSe_2$ alloy target (TASCO, 99.99% purity, 2-inch diameter) for a fixed set of process parameters after pre-sputtering for 5 minutes: an Ar gas flux of 20 sccm, a base pressure of 1.0×10^{-6} Torr, a substrate distance of 5.0 cm, an RF sputtering power of 35 watt, and a vacuum pressure of 7.5×10^{-3} Torr during the sputtering process for 2.5 minutes at room temperature. In (MTI Co. Inc., 99.99% purity, 2-inch diameter) and Ga (MTI Co. Inc., 99.99% purity, 2-inch diameter) were deposited on the $CuSe_2$ thin films by sputtering under the identical process conditions except for the RF sputtering powers of 20 Watt and 35 Watt for 20 seconds and 5 minutes, respectively. The average thickness of the In and Ga thin films were about 150 nm and 100 nm, as measured by using X-ray reflectometry (XRR). Table 1 shows the detailed

process conditions about this experiments.

A furnace or RTA was used for annealing the as-deposited samples. During the initial stage of the annealing treatment, each as-deposited sample was pre-heated in a tubular ceramic lab furnace for 10 minutes and then annealed at 400 or 600℃ for 1 hour in a vacuum ambient (~10^{-3} Torr). After the annealing treatment, the samples were kept in a vacuum chamber and slowly cooled to room temperature. RTA (Modular Process Technology Co., RTP-600S) treatment was also used for improving the temperature uniformity over the conventional furnace heating at 400℃ for 10 seconds in a N_2 gas ambient.

Table 1. Process conditions for sputtering and annealing

Sputtering Process Conditions	$CuSe_2$ Target	Power	35 W
		Time	150 sec
		Thickness	250 nm
	In Target	Power	20 W
		Time	20 sec
		Thickness	150 nm
	Ga Target	Power	35 W
		Time	300 sec
		Thickness	100 nm
	Vacuum		$7.5x10^{-3}$ Torr
	Ar		20 sccm
	Pre-sputtering Time		5 min
Annealing Process Conditions	Furnace	Temperature (Time)	400℃ (60 min)
		Temperature (Time)	600℃ (60 min)
	RTA	Temperature (Time)	400℃ (10 sec)

The crystalline structure of the thin films was analyzed using X-ray diffraction (XRD, Philips, X'pert-PRO-MRD, Cu Kα = 0.15405nm, 40kV, 30mA). The optical properties of the thin films were measured using a UV-visible spectrophotometer (Varian Techtron, Cary500scan) in the range of 400 - 800 nm. The electrical properties, including carrier concentration, resistivity and the mobility, of the thin films were characterized by using a Hall Effect measurement system (Accent Optical Technologies, HL5500PC) at room temperature.

B. Results and Discussion

Figure 17 shows the XRD patterns of the thin films of (a) $CuSe_2$, (b) as-deposited $CuSe_2$-In-Ga thin film, thin films annealed at (c) 400 or (d) 600℃ in the furnace, and (e) at 400℃ by RTA. The diffraction spectra were obtained by scanning 2Θ in the range of 10 - 90°.

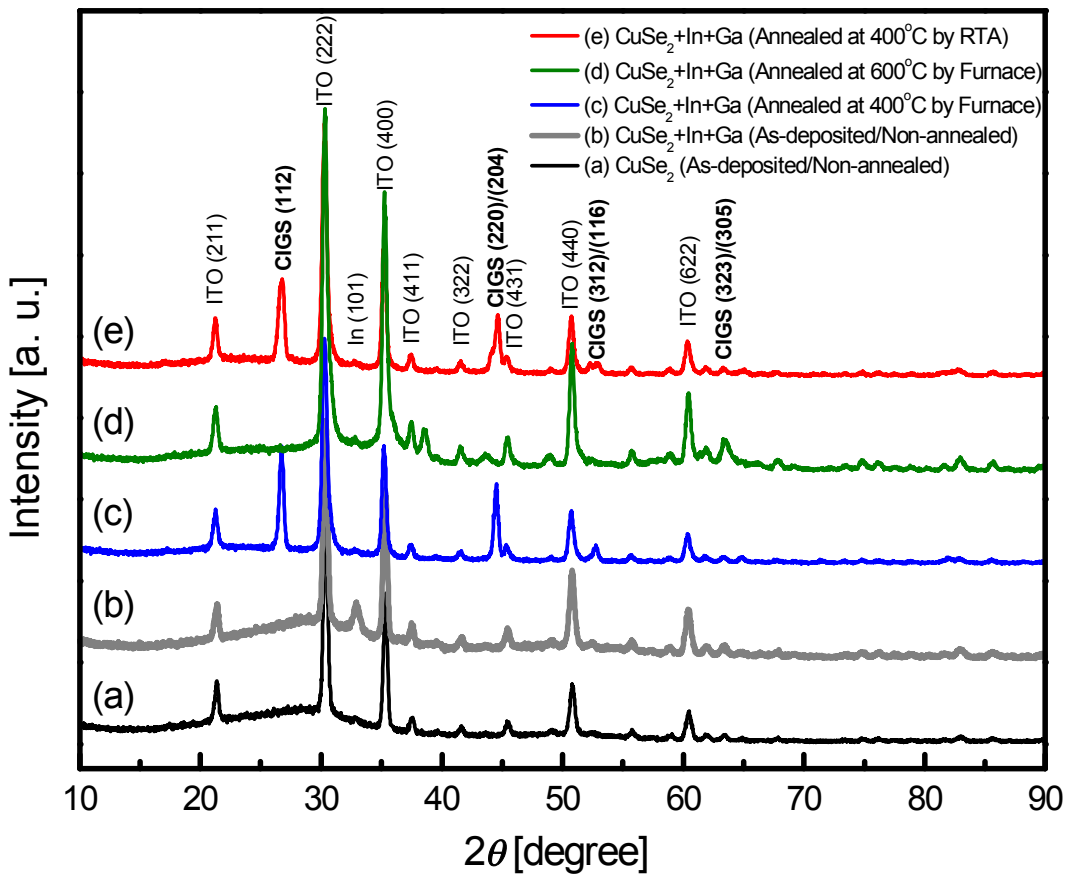

Fig 17. XRD patterns of the (a) as-deposited $CuSe_2$, the (b) as-deposited In and Ga on $CuSe_2$, the $CuSe_2$-In-Ga thin films annealed in a conventional furnace at (C) 400℃ and (d) 600℃, and the (e) thin film RTA-treated at 400℃

The diffraction pattern of the as-deposited $CuSe_2$ thin film shows the presence of (211), (222), (400), (411), (322), (431), (440), and (622) peaks at 2 θ = 21.35°, 30.39°, 35.27°, 37.45°, 41.59°, 45.39°, 50.79°, and 60.49°, respectively, correspond to ITO as the substrate in Fig. 1(a) [30,31]. The elemental In (101) peak appears at 2θ = 32.93° in the as-deposited $CuSe_2$-In-Ga thin films of Fig. 17(b) [7].

After the $CuSe_2$-In-Ga thin films were annealed at 400℃ for 1 hour in the furnace, the diffraction peaks of the preferred orientation are (112) at 2θ = 26.90°, (220)/(204) at 2θ = 44.71° and (312)/(116) at 2θ = 52.85°, corresponding to CIGS chalcopyrite phases [1,6,7,32]. The annealing treatment at 400℃ in the furnace without any ambient gas resulted in the chalcopyrite structures in the $CuSe_2$-In-Ga thin films. The intensities of the (220)/(204) and (312)/(116) diffraction peaks were sharper and stronger than the intensities reported in prior studies whereas that of the (112) peak was similar to the values [8,33], which means that this methodology can achieve crystallization quality and grain growth.

The (112), (220)/(204), and (312)/(116) diffraction peaks were not detected after the $CuSe_2$-In-Ga thin films had been annealed at a relatively higher temperature of 600℃ for 1 hour in the furnace, but the (323)/(305) diffraction peak occurred at 63.51° corresponding to the CIGS chalcopyrite phase [8,9,27].

This result coincided exactly with that of a previous study in which the XRD diffraction peaks gradually decreased when the annealing temperature further increased to 550℃ [6]. The electrical properties, including the opencircuit voltage (V_{oc}) and the short-circuit current density (J_{sc}), would be worsened in this condition because the densely packed (112), (220)/(224), and (312)/(116) oriented grains are known to reduce the carrier recombination and the leakage current due to the structural defects in the thin film [1].

Little or no change among the XRD diffraction patterns of the RTA-treated samples and annealed samples in the furnace at 400℃ was observed, as shown in Figure. 17 (c) and (e), which are due to (112), (220)/(204), and (312)/(116) chalcopyrite phases. RTA treatment would offer some advantages, such as

excellent control of stoichiometry through lower loss of In and lower thermal stress in the thin film at short reaction times and lower temperatures [34]; the further investigations of RTA treatment at lower temperature (<400℃) are required.

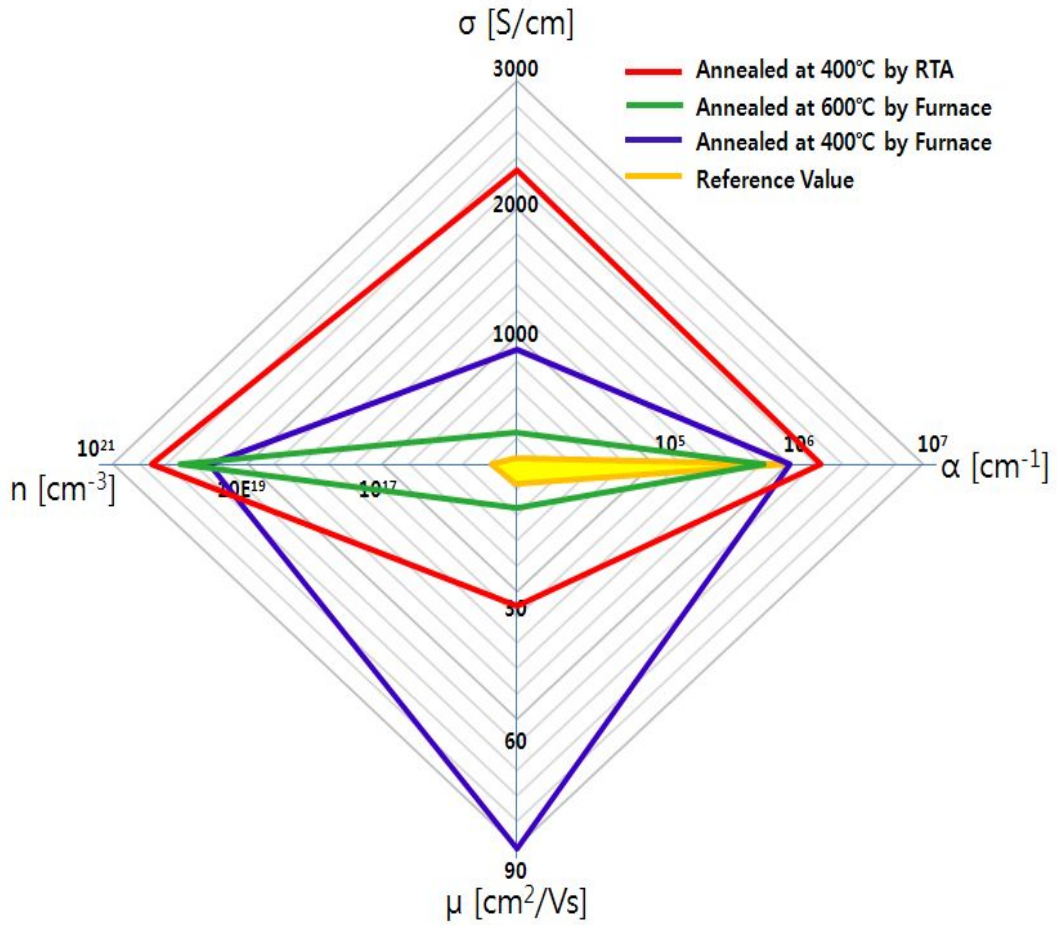

Fig 18. Conductivity (σ), carrier concentration (n), hole mobility (μ), and absorption coefficient (α) of the $CuSe_2$-In-Ga thin films annealed under various annealing condition in a conventional furnace at 400℃ and 600℃, and of the RTA-treated thin film at 400℃

Figure 18 shows the electrical and the optical properties of the annealed specimens. The conductivity (σ), carrier concentration (n), hole mobility (μ), and absorption coefficient (α) of the annealed $CuSe_2$-In-Ga thin films were measured and compared to the required or reported values in prior studies [5,35,36]. The absorption coefficient is a measure of how far an incident photon of given wavelength is absorbed below the surface of the thin film, that is, the ability of a semiconductor to absorb photons which was calculated by using Beer-Lambert's law [37,38].

The absorption coefficient of the CIGS films, as demonstrated by Han *et al.,* approached 10^5 cm^{-1}, which was consistent with the required value of the absorption coefficient [5] in the region of high photon energies regardless of the film thickness [35]. All absorption coefficients of the annealed $CuSe_2$-In-Ga thin films in this experiment were in a range from 8.24×10^5 to $2.41\times10^6 cm^{-1}$, which values are above the required value. The RTA-treated specimen showed the highest value whereas the specimen annealed in the furnace at 600℃ had the lowest value.

All conductivities of the annealed $CuSe_2$-In-Ga thin films in this experiment exceeded the reported values (0.22 S/cm) of the CIGS thin films with the same thickness (500 nm) to the above 3.34×10^2 S/cm [35]. The enhancement of the conductivity was more significant in the specimens annealed at 400℃; especially, its value was 2.33×10^3 S/cm in the RTA-treated specimen. All the annealed thin films showed p-type conductivity. The carrier concentration of the CIGS thin film was suggested to be more than 2×10^{16} cm^{-3}, which value was a relevant property of the NREL 19.9% device [36,39]. The measured values were on the order of 10^{19} - 10^{20} cm^{-3} in this experiment, which are very large compared to the required value. The carrier concentration achieved a maximum value of 4.43×10^{20} cm^{-3} in the RTA-treated specimen after sputtering with a $CuSe_2$ target.

The hole mobility of the CIGS thin films was around 4.25 cm^2/Vs in a prior study with the same thickness (500 nm) [35]. The hole mobility of the annealed $CuSe_2$-In-Ga thin films in this experiment showed a minimum value of

10.90cm^2/Vs and a maximum value of 90.10 cm^2/Vs for the samples treated in the furnace at 600℃ and 400℃, respectively. A higher hole mobility of 34.30 cm^2/Vs was obtained in the specimen RTA-treated at 400℃ compared to the specimen annealed in the furnace at 600℃ although the hole mobility showed the inverse tendency to the carrier concentration because the lower defect density in the thin film probably induced less phonon scattering in the RTA-treated specimen [40].

Ⅳ. CIGS Thin Films Sputtered by Using $CuSe_2$ with Multilayer-Stack-Structure and RTA

Considerable attention has been paid to thin film solar cells including polycrystalline copper indium gallium diselenide $CuIn_{1-x}Ga_xSe_2$ (CIGS) thin films with a chalcopyrite lattice structure as an absorber layer owing to its suitable optical absorption (> $10^5 cm^{-1}$), long-term electrothermal stability, high tolerance to defects, no toxic or hazardous pollutants, such as arsenic and cadmium, and a tunable band gap (1.04 – 1.68 eV) by adjusting the chemical composition ratio of Ga / (In + Ga) [1,2]. In a previous study, a novel method was proposed for preparing a chalcopyrite CIGS thin film without a selenization process by RF magnetron sputtering with In, Ga and $CuSe_2$ alloy targets [41]. The proposed method formed chalcopyrite (112), (220) / (204), and (312) / (116) phases by using either conventional annealing in a furnace or a RTA treatment at 400 °C without a selenium / sulfur containing gas. This process has many advantages including simplicity, large-area manufacturing for mass production, and excellent electrical and optical properties [41]. Another merit of this novel method is the ease of adjusting chemical composition ratio of Ga / (In + Ga) in CIGS thin films. In the present study, multilayer stack structured thin films with different thickness ratios were deposited.

A. Experimental Details

A commercial $CuSe_2$ alloy target (TASCO, 99.99% purity, 2inch diameter) was used for the preparation of $CuSe_2$ thin film on 2×2 cm Corning glass substrates. The thin films were deposited by RF magnetron sputtering (Vacuum Science Co.) using the following fixed set of process parameters after pre-sputtering for 5 minutes: An Ar gas flux of 20 sccm, base pressure of 1.0×10^{-6} Torr, substrate to distance of 5.0 cm, RF sputtering power of 35 watt, and vacuum pressure of

7.5×10^{-3} Torr during sputtering for 75 seconds at room temperature. An identical process was performed for subsequent sputter deposition of Ga and In layers on 125-nm-thick $CuSe_2$ thin films at RF sputtering powers of 35 and 20 watt, respectively. Commercial In (MTI Co. Inc., 99.99% purity, 2-inch diameter) and Ga (MTI Co. Inc., 99.99% purity, 2-inch diameter) targets were used to produce the Ga / In / $CuSe_2$ multilayer stack structure. The total thickness of the Ga and In thin films was approximately 125 nm, as measured by X-ray reflectometry (XRR). The Ga / (In + Ga) thickness ratio was varied from 0.2 to 0.5 with an interval of 0.1. The deposition rates of Ga and In were 10 and 300 nm/minute, respectively. Subsequently, 125-nm-thickness $CuSe_2$ thin films were deposited on the stacked thin films using the above fixed set of process parameters for 75 seconds dissimilarly to our previous study [41]. Annealing of the stacked samples resulted in the formation of CIGS chalcopyrite (112), (220) / (204), and (312) / (116) phases in either a conventional furnace or by RTA at 400°C without a selenium / sulfur containing gas, as reported elsewhere [41].

Table 2. Process conditions for sputtering and RTA

Sputtering Process Conditions	$CuSe_2$ Target	Power	35 W
	In Target	Power	20 W
	Ga Target	Power	35 W
	Vacuum		$7.5x10^{-3}$ Torr
	Ar		20 Sccm
	Pre-sputtering Time		5 min
RTA Process Conditions	Temperature (Time)		400℃ (10 sec)

Table 3. TSputtering Times for each target for maintaining total thickness with a change of Ga / (In + Ga) thickness ratio in multilayer-stack-structure

In : Ga / Layer	0.8 : 0.2 Thickness (Time)	0.7 : 0.3 Thickness (Time)	0.6 : 0.4 Thickness (Time)	0.5 : 0.5 Thickness (Time)
$CuSe_2$	125 nm (75 sec)	125 nm (75 sec)	125 nm (75 sec)	125 nm (75 sec)
In	200 nm (40 sec)	175 nm (35 sec)	150 nm (30 sec)	125 nm (25 sec)
Ga	50 nm (300 sec)	75 nm (450 sec)	100 nm (600 sec)	125 nm (750 sec)
$CuSe_2$	125 nm (75 sec)	125 nm (75 sec)	125 nm (75 sec)	125 nm (75 sec)

The RTA (Modular Process Technology Co., RTP-600S) treatment of the 400-nm-thick $CuSe_2$/Ga/In/$CuSe_2$ stacked samples was performed to improve the temperature uniformity over conventional furnace heating at 400 °C for 10 seconds in N_2 gas ambient. The crystalline structure of the thin films was analyzed by X-ray diffraction (XRD, Philips, X'pert-PRO-MRD, Cu Kα = 0.15405 nm, 40 kV, 30 mA). The optical properties of the thin films were measured using an UV-visible spectrophotometer (Varian Techtron, Cary500scan) in the range of 400 - 1500 nm. The electrical properties of the thin films, including the carrier concentration, resistivity and the mobility, were characterized using a Hall Effect measurement system (Accent Optical Technologies, HL5500PC) at room temperature. X-ray photoelectron spectroscopy (XPS, Multilab 2000, Thermo VG Scientific) surface analyses of the RTA-treated samples were performed using a monochromatic (1486.6 eV). A take-off angle of 90° was used for allanalyses. For the high-resolution spectra, the binding energies were referenced to the C 1s peak at 285.0 eV.

B. Results and Discussion

Figure 19 shows XRD patterns of the RTA-treated $CuSe_2$/Ga/In/$CuSe_2$ stacked specimens with different Ga / (In + Ga) thickness ratios; (a) 0.2, (b) 0.3, (c) 0.4, and (d) 0.5. The XRD patterns were obtained by scanning 2Θ in the range of 15 - 75°. All the RTA-treated stacked thin films showed the major diffraction peaks corresponding to CIGS chalcopyrite phases with a preferred orientation: (112), (220)/(204) and (312)/(116) at 2Θ = 26.63°, 44.47° and 52.47° [1,6,7,32,41]. This confirms that this method can achieve excellent crystallization quality and grain growth. Sufficient electrical properties including the open circuit voltage (V_{oc}) and short circuit current density (J_{sc}) can be obtained by reducing the carrier recombination and structural defect-originated leak age current in the thin films by the densely packed (112), (220)/(224), and (312)/(116)-oriented grains [1].

Weak diffraction peaks of (323)/(305) and (332)/(316) were observed at 2Θ = 64.15° and 70.91° corresponding to a CIGS chalcopyrite phase [6,7,33,41]. The XRD pattern of all specimens did not indicate the presence of noticeable peaks except for the CIGS-based chalcopyrite peaks, as shown in Figure 19.

The intensities of the major (112), (220)/(204), and (312)/(116) peaks increased with decreasing Ga / (In + Ga) thickness ratio from 0.5 to 0.3, and then decreased slightly at a thickness ratio of 0.2, as shown in the inset in Figure 19 indicating the normalized intensity. A similar trend of intensity was observed for each case of all the CIGS-based peaks and only (112) peak. This means that the crystallinity of CIGS films increased with decreasing Ga / (In + Ga) thickness ratio from 0.5 to 0.3.

The full width at half maximum (FWHM) of (220)/(204) and (312)/(116) peaks decreased with decreasing Ga / (In + Ga) thickness ratio from 0.5 to 0.3, as shown in Figure 20, whereas the sharp and strong (112) peak showed no significant difference in the FWHM with decreasing thickness ratio, which indicates an increase in grain size of the CIGS thin films. The FWHM is affected

directly by the Ga concentration due to a distortion of the chalcopyrite lattice structure resulting from the incorporation of Ga into the In sites [42,43].

Moreover, both peaks corresponding to the (220)/(204) and (312)/(116) orientations shifted to lower 2Θ values with decreasing Ga / (In + Ga) thickness ratio (Figure 20), which is consistent with the well-known shift in the diffraction peaks to a higher angle with increasing Ga content due to the decrease in the 'a' and 'c' lattice constants. Hence, the d spacing increases with the replacement of the larger In atoms with smaller Ga atoms [33,42-44]. Therefore, XRD suggests that polycrystalline CIGS was rebuilt on the substrate, and the crystallinity could be modified by changing the thickness ratio of the multilayer-stacked thin films.

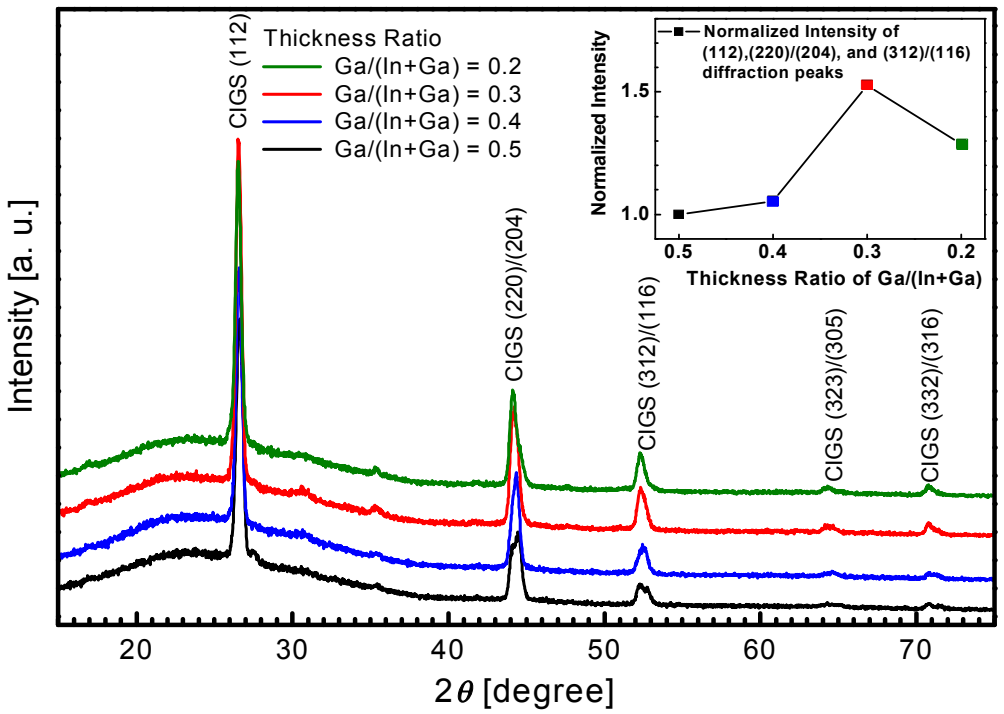

Fig. 19 XRD patterns of the RTA-treated specimens with different Ga / (In + Ga) thickness ratios from 0.5 to 0.2. The inset shows the normalized XRD intensity of (112), (220)/(204), and (312)/(116) phases in the RTA-treated specimens as the same change in thickness ratio

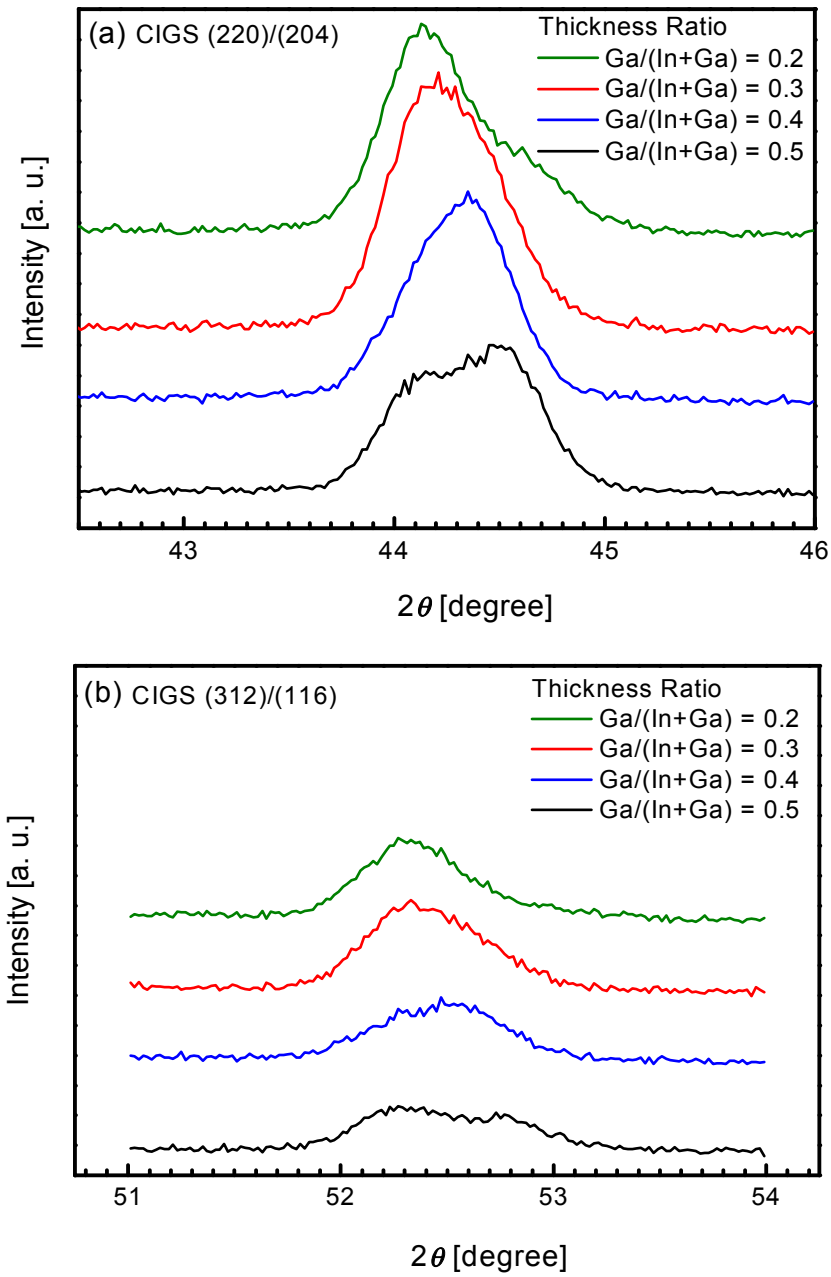

Fig. 20 Magnification of the (a) CIGS (220)/(204) and (b) CIGS (312)/(116) XRD peaks in the RTA-treated specimens with different Ga / (In + Ga) thickness ratios

The optical band gap energy (Eg) of the RTA-treated samples was estimated by a linear extrapolation of each curve back to the energy axis from the Tauc plot of $(\alpha h\upsilon)^2$ vs. the photon energy ($h\upsilon$), as shown in Figure 21, where α is the absorption coefficient, h is Plank's constant and υ is the frequency of the incident photon. All the estimated optical band gap energies (E_g = 1.73 - 1.88 eV) were higher than the reported values(E_g = 1.04 - 1.68 eV) [1].

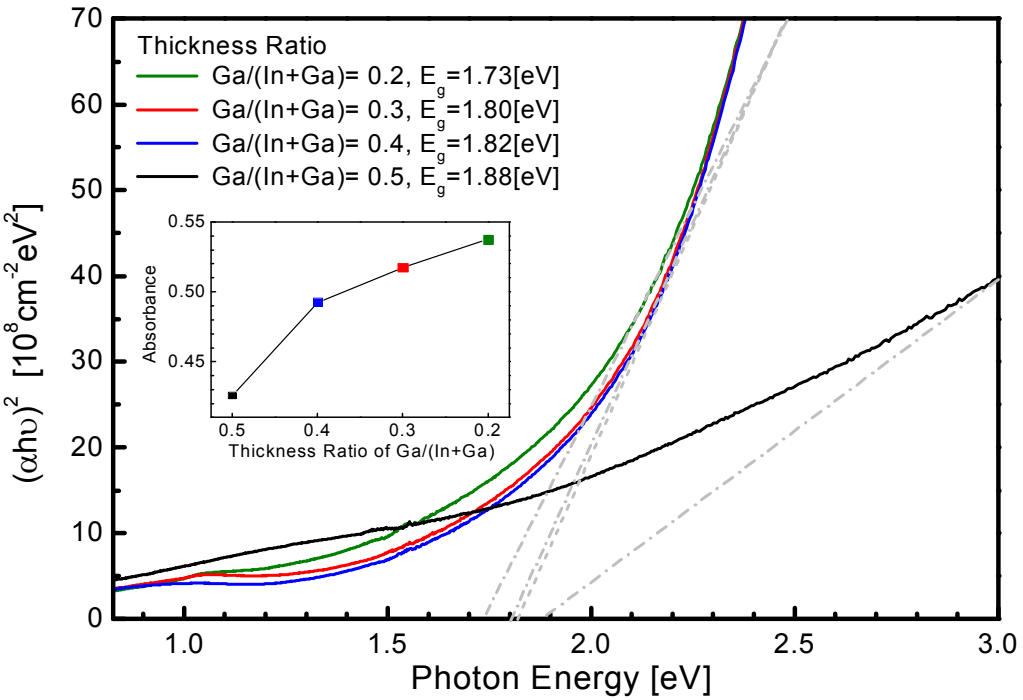

Fig. 21 Tauc plot of $(\alpha h\upsilon)^2$ vs. the photon energy ($h\upsilon$) for the RTA-treated CIGS thin films with decreasing Ga / (In + Ga) thickness ratio from 0.5 to 0.2. The optical band gap energies were estimated through a linear extrapolation of each curve back to the energy axis. The inset shows the average absorbance in the range of 400 -1500 nm with the same change

XPS surface analyses attributed this phenomenon to the Cu-poor (Cu / (In + Ga) < 0.8) and Ga-rich (Ga / (In + Ga) > 0.8) compositions of all the

RTA-treated thin films *(not shown)*. Note that the highest conversion efficiency was acquired by varying the composition: 0.80 < Cu / (In + Ga) < 0.92 and 0.30 < Ga / (In + Ga) < 0.35 [3]. The optical band gap energy of Cu-poor (Cu / (In + Ga) < 1) thin films is generally higher than that of the stoichiometric (Cu / (In + Ga) = 1) thin films [44,45]. Because the optical band gap energy of CIGS thin films can be controlled by adjusting the chemical composition ratio of Ga / (In + Ga), the larger chemical composition ratio of Ga / (In + Ga) results in a higher optical band gap energy [44,46]. This innovatively devised method is still unable to control the chemical composition ratio of Ga / (In + Ga) completely by quantifying the thickness ratio. Nevertheless, further studies will overcome this problem with the optimum annealing process [6].

The well-known tendency to increase in the optical band gap energy was observed with increasing Ga / (In + Ga) thickness ratio, which confirmed that the thickness ratio can be used to control the chemical composition ratio of Ga / (In + Ga) in CIGS thin films [47,48]. The absorbance at a certain wavelength of light can be calculated using the formula: $A = -\log T = \log I_0/I$, where A is the absorbance, T is the transmittance, I_0 is the intensity of incident radiation, and I is the intensity of transmitted radiation. The average absorbance in the range of 400 - 1500 nm was approximately 0.5, as shown in the inset in Figure 21, which means that approximately 70% of incident radiation can be absorbed by 400-nm-thick thin films because the absorbance can be enhanced by adjusting the chemical composition ratio of Ga / (In + Ga) [49]. Nevertheless, more study will be needed.

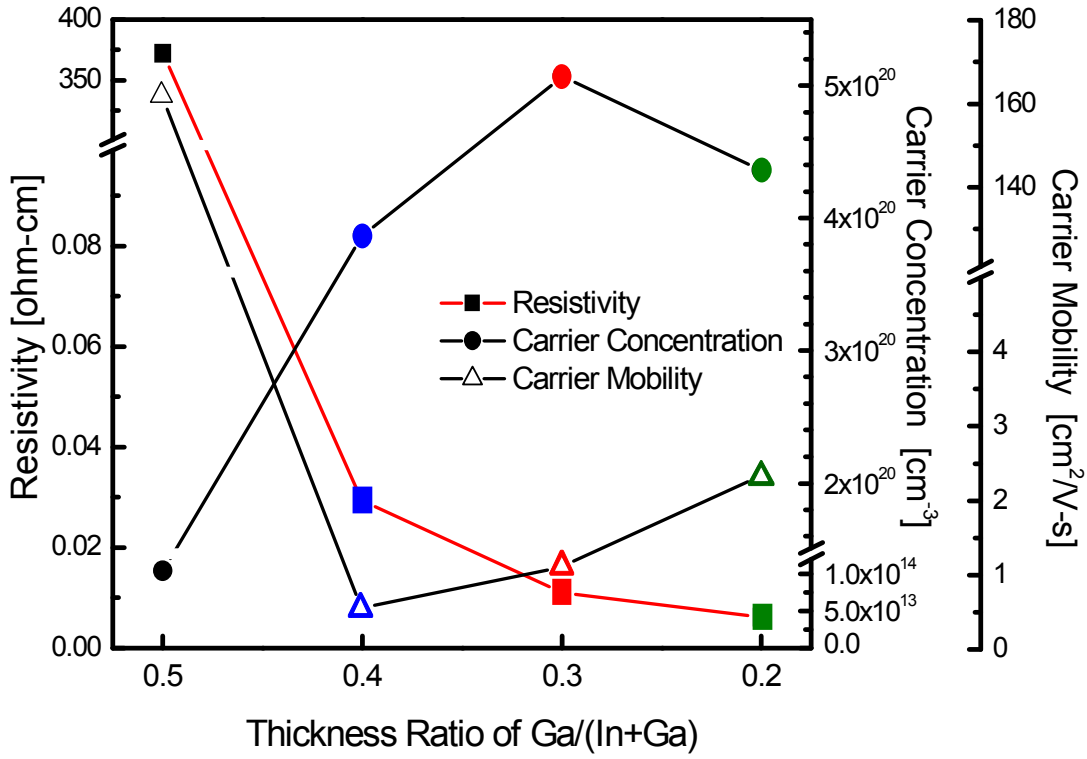

Fig. 22 Resistivity (ρ), carrier concentration (n), and carrier mobility (μ) of the RTA-treated CIGS thin films with decreasing Ga / (In + Ga) thickness ratio

Figure 22 shows the effects of the Ga / (In+Ga) thickness ratio on the electrical properties of the RTA-treated thin films including resistivity (ρ), carrier mobility (μ) and carrier concentration (n) determined by Hall Effect measurements. All the RTA-treated thin films in this experiment exhibited p-type conductivity according to Hall Effect measurements. The resistivity decreased and the carrier concentration increased with decreasing Ga / (In+Ga) thickness ratio. The resistivity of the RTA-treated thin film was 3.72×10^{2} Ω-cm at a Ga / (In+Ga) thickness ratio of 0.5. The resistivity reached a minimum value of 6.15×10^{-3} Ω-cm at a Ga / (In+Ga) thickness ratio of 0.2.

The carrier mobility decreased rapidly with decreasing Ga / (In+Ga) thickness

ratio from 0.5 to 0.4 due to the considerable increase in carrier concentration. The carrier mobility increased with decreasing Ga / (In+Ga) thickness ratio from 0.4 to 0.3. The decrease in carrier scattering and increase in carrier mobility related to the decrease in resistivity was attributed to the better crystallinity and larger grains on the thin film surface [6], which also agrees with the FWHM results from XRD analysis. The reduced resistivity would improve the short circuit current density and fill factor (FF) in the solar cell due to the decreased series resistance of the thin films [43]. The required carrier concentration of CIGS thin films is more than 2×10^{16} cm^{-3}, which is the relevant property of the NREL 19.9%-efficient device [36,39]. The carrier concentration of the RTA-treated thin film was in the order of 10^{14} cm^{-3} at a Ga / (In+Ga) thickness ratio of 0.5, which is insufficient for the suggested value. On the other hand, the carrier concentration increased significantly to the order of 10^{20} cm^{-3} at Ga / (In+Ga) thickness ratio < 0.4. The decreased grain boundaries, which act as recombination centers [50], resulted in an increase in carrier concentration in the RTA-treated thin film at a Ga / (In+Ga)thickness ratio < 0.4 due to the decreased recombination of photogenerated electrons [51,52]. The maximum value was 5.07×10^{20} cm^{-3}, which exceeds the required value.

Ⅴ. Application of Laser Annealing to Preparation for Polycrystalline CIGS Thin Film

Laser annealing of semiconductors has some advantages, such as localized high temperatures with excellent annealing selectivity to the underlayers or substrate for a short duration [12,13]. Thin flim solar cells require a selective annealing process with the use of multilayered and heterojunctioned stucture to avoid interdiffusion with the underlayers or substrate during the annealing process. In a previous study, a novel method was proposed for preparing a chalcopyrite CIGS thin film without a selenization process by RF magnetron sputtering with In, Ga and $CuSe_2$ alloy targets [16]. However, applying of laser annealing is required in the multi-layer structures CIGS thin films. In this chapter, a continuous wave 532-nm laser was used to grow the grains and improve the crystallization of CIGS thin films. The effect of laser annealing on the CIGS thin films was examined at different laser powers in the laser annealing process by analyzing the structural, the optical and the electrical properties of CIGS thin films.

A. Experimental Details

In this chapter, the thin films were deposited by RF magnetron sputtering (Vacuum Science Co.) using the following fixed set of process parameters after pre-sputtering for 5 minutes. The RF sputtering method was employed by using a commercial $CuSe_2$ alloy target (TASCO, 99.99% purity, 2-inch diameter), In (MTI Co. Inc., 99.99% purity, 2-inch diameter) and Ga (MTI Co. Inc., 99.99% purity, 2-inch diameter) targets. These were deposited on a $2\times2cm^2$ corning glass in vacuum chamber with a fixed process condition, as shown in Table 4.

Table 4. Process condition in sputtering

Sputtering Process Conditions	$CuSe_2$ Target	Power	35 W
		Time	150 sec
		Thickness	250 nm
	In Target	Power	20 W
		Time	20 sec
		Thickness	150 nm
	Ga Target	Power	35 W
		Time	300 sec
		Thickness	100 nm
	Vacuum		$7.5x10^{-3}$ Torr
	Ar		20 sccm
	Pre-sputtering Time		5 min

The deposited thin films had a $CuSe_2$ / In / Ga layer-structure with the total thickness of 500 nm. These thin films were annealed by using annealing method. A Nd:YAG module (LTS Co., Ltd., Verdi-V 18), which has the beam size and laser speed of 50μm and 1 mm/sec, respectively, was mounted in a thermoelectric cooler as a heat sink with the maximum output power of approximately 10 W at 532 nm. The laser irradiation was scanned by a Galvanometric mirror for 10 seconds which corresponded to the scanning velocity of 667 mm/s. The laser annealing process with a continuous-wave (CW) green laser (532 nm) supplied a sufficient energy to dissolve and activate each layer of the sputtered $CuSe_2$ / In / Ga thin films to product $Cu(In,Ga)Se_2$ compound. The laser power was controlled from 3.0 to 3.4 watt with an interval of 0.2 watt. The detailed conditions of the laser annealing is summarized in Table 5.

Table 5. Process parameters in laser annealing

Laser Annealing Process Condition	Wavelength	532 nm
	Beam size	50 μm
	Laser Speed	1 mm/sec
	Exposure Time	10 sec
	Width of laser duplication	20 μm
	Laser power	Non-annealed
		3.0 W
		3.2 W
		3.4 W

The crystal structure of thin films was analyzed by using X-ray diffraction (XRD) after laser annealing process. The optical properties and electrical characteristics of the as-deposited and laser annealed Cu(In,Ga)Se_2 thin film were analyzed by using an UV-isible spectrophotometer and a Hall Effect measurement system.

B. Results and Discussion

Figure 23 shows the XRD patterns of CIGS thin films (a) non-annealind (b) laser annealed at 3.0, (c) 3.2 and (d) 3.4 watt. The XRD patterns were obtained by scanning 2Θ in the range of 20-80°. The diffraction pattern of non-annealed CIGS thin film shows the presence of (110), (220), (110), (312)/(116) and (323)/(305) peaks at 2Θ = 32.96°, 35.74°, 39.17° 54.39°, and 63.20°, respectively. However the (112) and (220)/(204) peaks of CIGS chalcopyrite phase was not observed in the as-deposited spicemen. Laser annealed CIGS thin films show the presence of the (112) peaks at 3.0 and 3.2 watt.

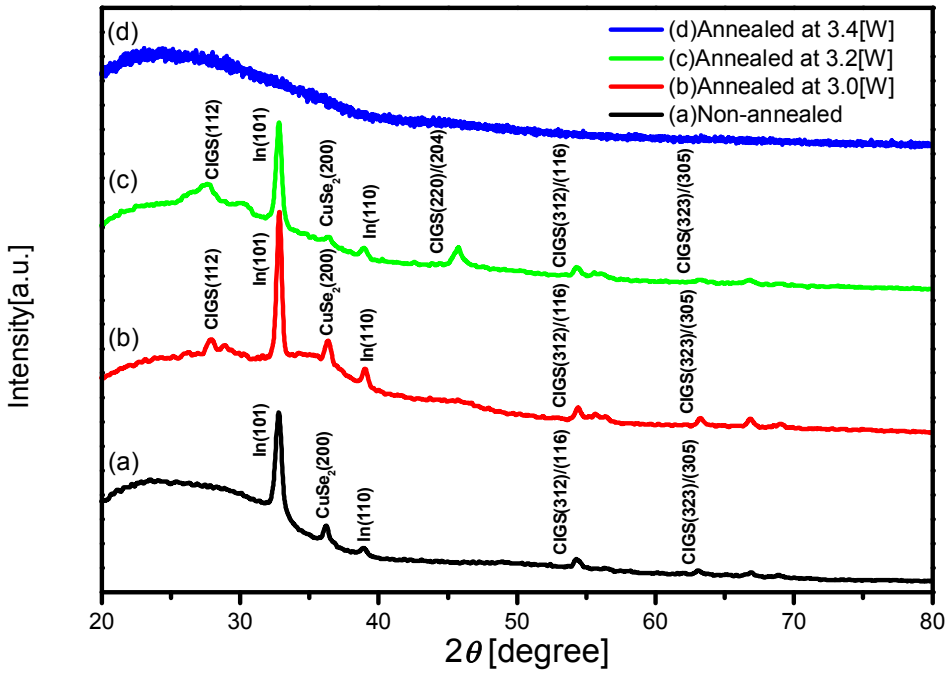

Fig. 23 XRD patterns of (a) the non-annealed, the laser-annealed by (b) 3.0, (c) 3.2, and (d) 3.4 watt on the $CuSe_2$ / In / Ga layer-structured thin films

On the other hand, laser annealed CIGS thin film at 3.2 watt shows the presence of (112), (220)/(204), (312)/(116) and (323)/(305), corresponding to CIGS chalcopyrite phases [1,6,7,32]. However, laser annealed CIGS thin film was not shown any peak at 3.4 watt. Any peak related to the CIGS chalcopyrite phase did not appear, which means that the microstructure became amorphous. These results prove that the structural properties of CIGS thin films were changed by laser annealing power with generating the amorphous thin film when the laser annealing power was greater than the threshold. Therefore, XRD suggests that polycrystalline CIGS was rebuilt on the substrate, and the crystallinity could be modified by changing the laser power.

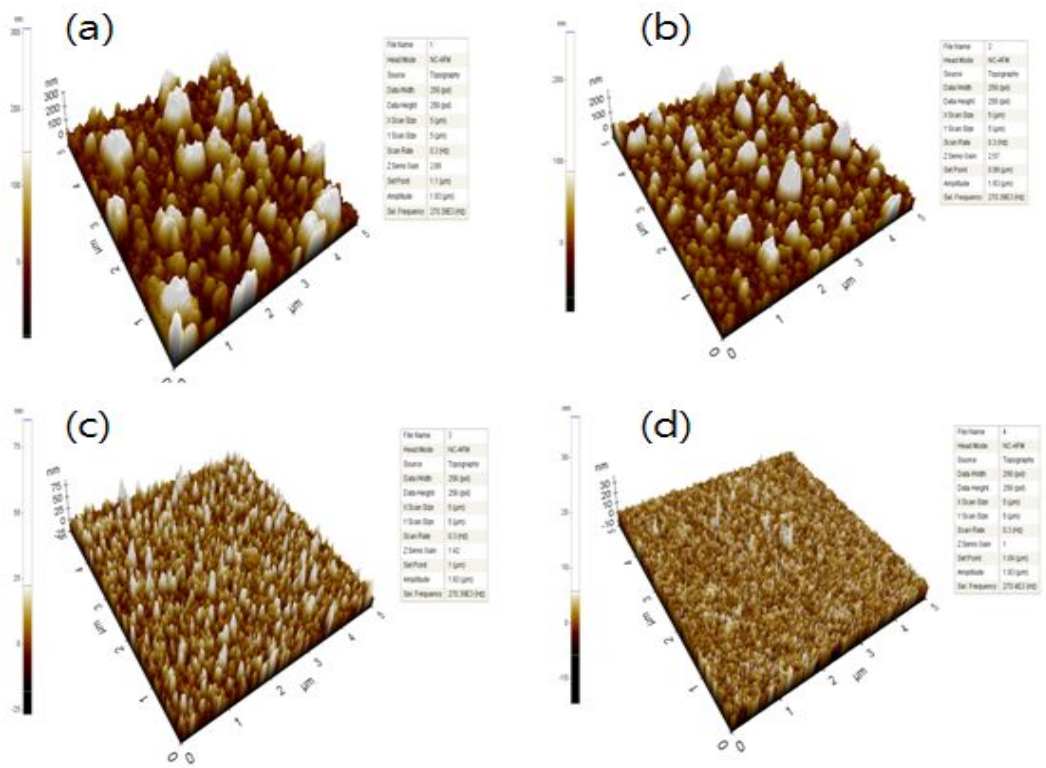

Fig 24. AFM 3D images of (a) the non-annealed, (b) 3.0, (c) 3.2, and (d) 3.4 watt on the $CuSe_2$ / In / Ga layer-structured thin films

Atomic force microscopy (AFM, Park System, XE-100) was used to measure the surface morphology of the CIGS thin films in non-contact mode. The AFM 3D images in Figure 24 show that the crystallinity of the CIGS thin films by changing laser annealing power. The grain size is generally affected by the annealing temperature because the crystallographic rearrangement for the coalescence of small grain into large grains in thin films in driven by the annealing temperature [53,54]. This suggests that the output power in laser annealing can be used as a proper parameter to control the surface temperature, which is similar to adjusting the annealing temperature in the conventional annealing process [55,56]. These results coincide with the AFM measurements of the surface morphologies of the CIGS thin films. The surface morphology of laser-processed absorbers as visualised by AFM is shown in Figure 24, which were produced with laser power from 3.0 to 3.4 watt. The annealed thin films at 3.4 watt showed that grain size was very small with no XRD peak, as shown in Figure 23. One simple reason of this is by carrying out the laser doping at higher laser energies to deliberately create some ablation [57].

Figure 25 presents the absorption coefficient (α) of the CIGS thin films, which was calculated using the Beer-Lambert's law in the high absorption region [58,59]: $\alpha(v) = (2.303/d)A$, where α(v), d and A are the absorption coefficient, film thickness and film absorbance, respectively. The absorption coefficient of CIGS thin films was located on the large wavelength in the visible spectral region (400 - 800 nm). The absorption coefficient of laser annealed and non annealed CIGS thin films remain near 10^8 cm^{-1}, among them the annealed thin film at 3.4 watt was the highest value.

The optical band gap energy (E_g) of the RTA-treated samples was estimated by a linear extrapolation of each curve back to the energy axis from the Tauc plot of $(\alpha h\upsilon)^2$ vs. the photon energy ($h\upsilon$), where α is the absorption coefficient, h is Planck's constant (4.135667×10^{15} eV_s) and ν is the frequency of the incidient photon [60]. All the estimated optical band gap energies (E_g = 1.23 - 1.302 eV) were included in the reported values (E_g = 1.04 - 1.68 eV) [1]. The

optical band gap energy of the CIGS thin films increased with the increasing laser power. The optical band gap energy of CIGS thin films can be controlled by the laser annealing power.

All the thin films in this experiment exhibited p-type conductivity according to Hall Effect measurements. Laser annealed and non-annealed thin films including resistivity (ρ), carrier mobility (μ) and carrier concentration (n) determined by Hall Effect measurements. The resistivity increased with increasing laser power up to 3.4 watt and the carrier concentration decreased with increasing laser power until 3.2 watt as shown in Figure 26. The carrier concentration increased rapidly at 3.4 watt annealed thin film. The resistivity of the non-annealed thin film was 1.665×10^{-3} Ω-cm. The resistivity reached a minimum value of 5.432×10^{-2} Ω-cm at annealed 3.4 watt.

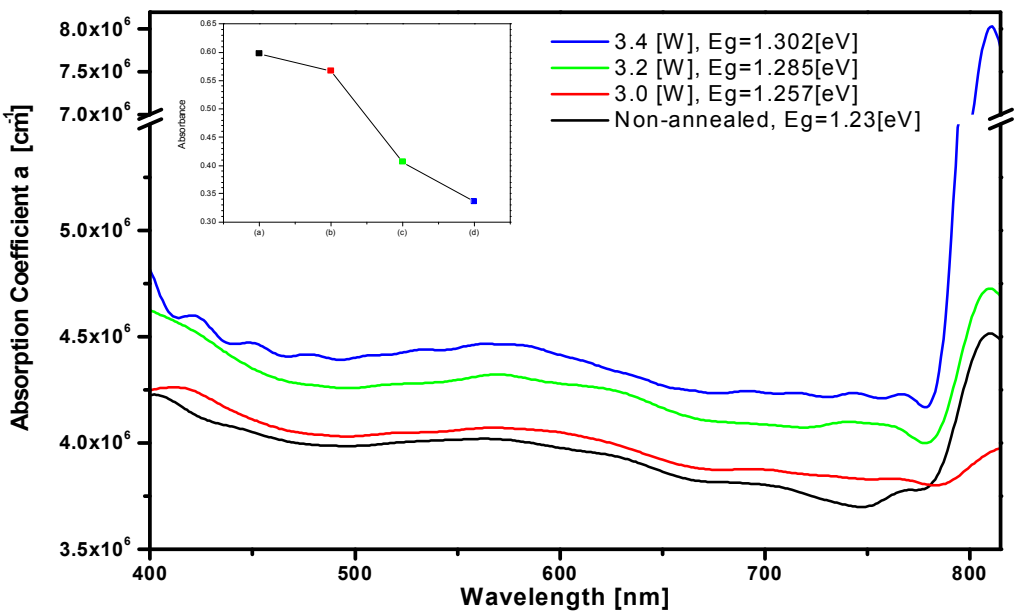

Fig. 25 Absorption coefficient spectra for specimens of (a) the non-annealed, (b) 3.0, (c) 3.2, and (d) 3.4 watt on the $CuSe_2$ / In / Ga layer-structured thin films

The carrier mobility decreased rapidly from non-annealed thin film to laser annealed thin film at 3.0 watt due to the considerable increase in carrier concentration. The carrier mobility decreased with increasing laser power. The decrease in carrier mobility related to the increase in resistivity was attributed to the better crystallinity and larger grains on the thin film surface [6]. The required carrier concentration of CIGS thin films is more than 2×10^{16} cm^{-3}, which is the relevant property of the NREL 19.9%-efficient device [42,45]. The carrier concentrations of the laser annealed thin film were in the order of 10^{22} cm^{-3}, which are significantly better than the suggested value.

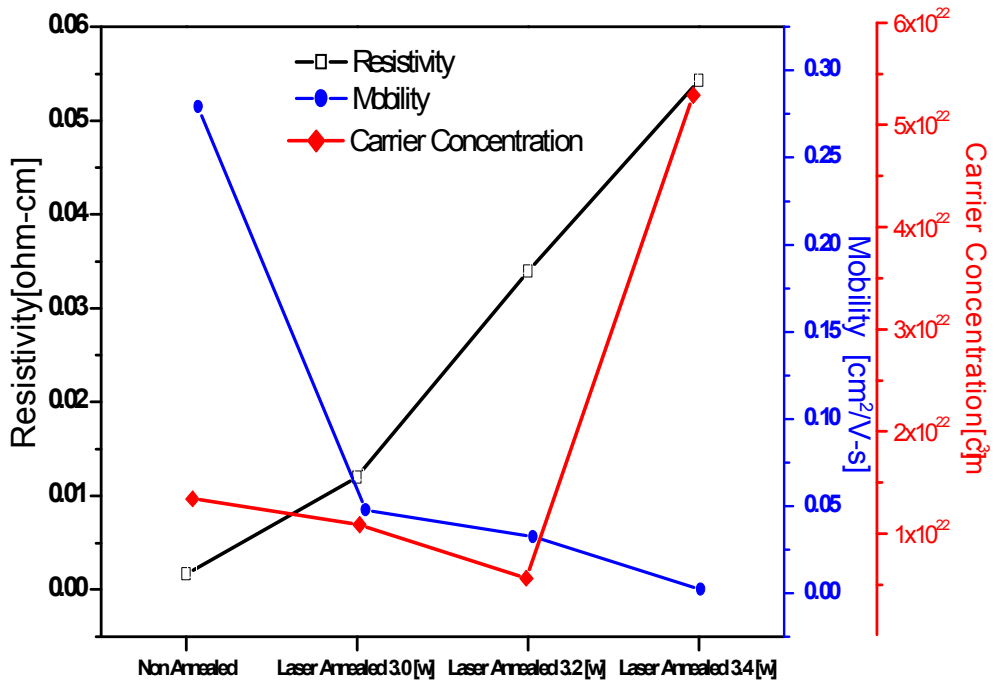

Fig. 26 Resistivity (ρ), carrier concentration (n), and carrier mobility (μ) of (a) the non-annealed, (b) 3.0, (c) 3.2, and (d) 3.4 watt on the $CuSe_2$ / In / Ga layer-structured thin films

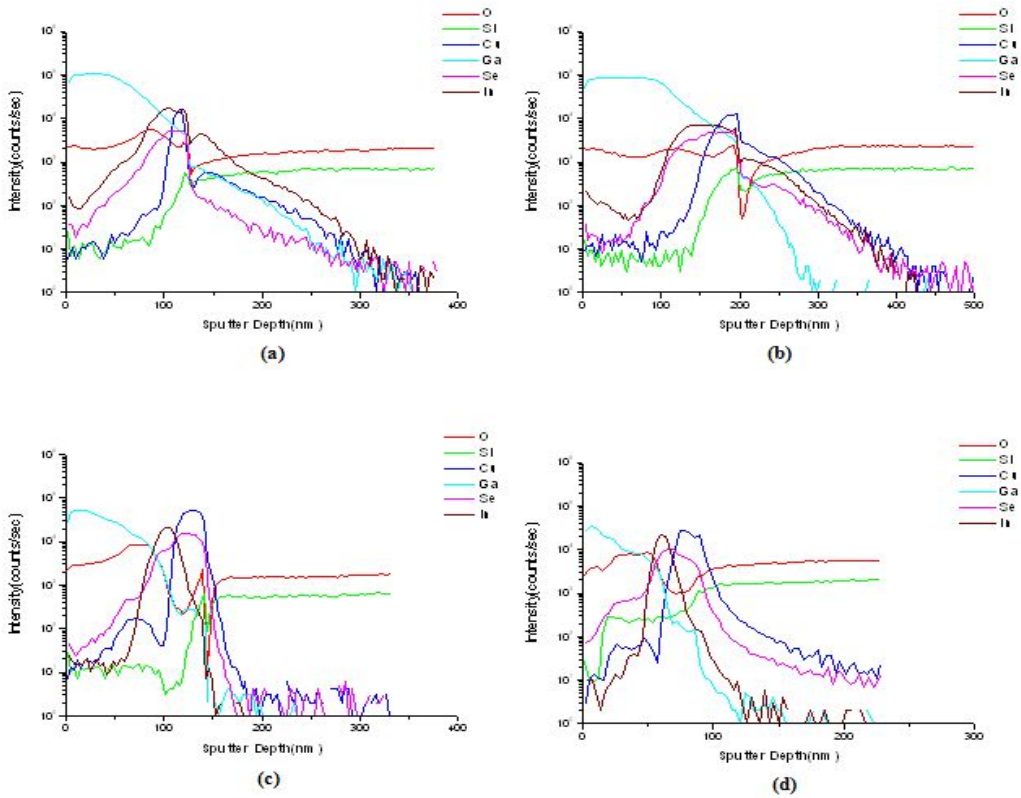

Fig.27 SIMS depth profiles of (a) the non-annealed, (b) 3.0, (c) 3.2, and (d) 3.4 watt on the $CuSe_2$ / In / Ga layer-structured thin films

Secondary ion mass spectrometry (SIMS, CAMECA SAS., IMS 6f Magnetic Sector SIMS) depth profile analyses of the laser annealed samples were performed using a typical Cs+ primary ion of 5 keV impact energy, an incident angle of 45° to normal, a beam current of 20 nA and a raster area of 200 × 200 μm. The depth profiles of the different CIGS samples were obtained with a SIMS instrument, as shown in Figure 27. SIMS depth profiles show that the Cu / In ratio was decreased with increasing the laser power. In contrast, In / Ga ratio showed no remarkable change compare with Cu / In ratio. The drawback in conventional process by using the electric furnace or RTA was the Se-loss, which have to insert He_2Se gas in annealing process. However, the laser annealing process in this thesis showed no Se-loss regardless of laser power.

On the other hand, the annealed samples at 3.2 and 3.4 watt were diffused at the near surface of CIGS thin films. It prove that the laser annealing power affected to the depth profiles of CIGS thin films

Ⅵ. Conclusion

A non-selenization method for preparing CIGS thin films by using sputtering deposition with a $CuSe_2$ target was suggested. The CIGS chalcopyrite (112), (220)/(204), and (312)/(116) phases were successfully formed by annealing in a conventional furnace and RTA at 400℃ without any selenium-/sulfur-containing gas. The conductivity, carrier concentration, hole mobility, and absorption coefficient of all the annealed thin films were considerably superior to the required or reported values. The stable properties obtained for RTA at a lower temperature and shorter holding time are as follows: a conductivity of 2.33 × 10^3 S/cm, a carrier concentration of 4.43 × 10^{20} cm^{-3}, a hole mobility of 34.30 cm^2/Vs, and an absorption coefficient of 2.41 × 106 cm^{-1}. This proposed method is expected to produce high-quality CIGS thin films with mass production for photovoltaic applications.

In this thesis reported a new non-selenization method for preparing CIGS thin films by the sputtering deposition of multilayer stack structured thin films using a $CuSe_2$ alloy target followed by a RTA treatment. The CIGS chalcopyrite (112), (220)/(204), and (312)/(116) phases were formed by the RTA treatment at 400°C for 10 seconds. The XRD peaks of the RTA-treated CIGS thin films became stronger, narrower, and shifted to lower 2θ values with decreasing Ga/(In+Ga) thickness ratio, which confirmed the enhanced crystallinity and grain size of the RTA-treated CIGS thin films. The optical band gap energy was in the high range of 1.73-1.88eV and the average absorbance was approximately 0.5 in the range of 400-1500 nm due to the Cu-poor and Ga-rich compositions of the thin films. Nevertheless, more study will be needed because these values could be controlled by adjusting the Ga/(In+Ga) thickness ratio. The resistivity, carrier mobility and carrier concentration of the CIGS thin films were $6.15\times10^{-3}\Omega$-cm, 2.33 cm^2/Vs and $5.07\times10^{16}cm^{-3}$, respectively, which are good or acceptable values for high quality CIGS thin film solar cells. The Hall Effect measurements were also affected by the proportion of Ga in the total thickness of In and Ga.

Overall, this novel non-selenization process can be used to prepare the CIGS thin films, and the film characteristics can be controlled by adjusting the thickness ratio.

The last chapter covered the application of laser annealing on CIGS thin films. CIGS thin films were deposited by multi stacked sputtering method using a $CuSe_2$ alloy target and these thin films were annealed by using annealing method. A Nd:YAG module, which has the beam size and laser speed of 50μm and 1 mm/sec, respectively. The CIGS chalcopyrite (112), (220)/(204), and (312)/(116) phases were formed by analysis of XRD but the surface of thin films occurred the ablation when laser power is over 3.4[watt]. As a result, the threshold power for laser annealing on CIGS thin film was known. The estimated optical band gap energies (E_g = 1.23 - 1.302 eV) were included in the reported values (E_g = 1.04 - 1.68 eV) and the optical band gap energy of CIGS thin films can be controlled by the laser annealing power. Moreover, the resistivity increased with the increasing laser power, which was 2.7×10^{-1} Ω-cm at non-annealed thin film and the minimum value was 2.17×10^{-3} Ω-cm at annealed 3.4[watt]. In addition, SIMS depth profiles show that the sputter depth (nm) were decreased with increasing the laser power. It prove that the laser annealing power affected to the depth profiles of CIGS thin films. In this chapter, the applicability of laser annealing was confirmed by the structural, electrical, optical and chemical analysis.

These novel processes can be manufactured with high efficiency and expected to obtain a high quality CIGS thin film solar cell.

Reference

[1] B.T. Jheng, P.T. Liu, M.C. Wu, H.P.D. Shieh, Opt. Lett. 37 (2012) 2760.

[2] Y.C. Lin, J.H. Ke, C.C. Chen, Appl. Mech. Mater. 189 (2012) 63.

[3] P. Jackson, D. Hariskos, E. Lotter, S. Paetel, R. Wuerz, R. Menner, W. Wischmann, M. Powalla, Prog. Photovolt. Res. Appl. 19 (2011) 894.

[4] O. Schultz, S. W. Glunz, G. P. Willeke, Prog. Photovolt. Res. Appl. 12 (2004) 553.

[5] T. M. Razykov, C. S. Ferekides, D. Morel, E. Stefanakos, H. S. Ullal, H. M. Upadhyaya, Sol. Energy 85 (2011) 1580.

[6] Y.C. Lin, Z.Q. Lin, C.H. Shen, L.Q. Wang, C.T. Ha, C. Peng, J. Mater. Sci. 23 (2012) 493.

[7] C.M. Xu, Y. Sun, L. Zhou, F.Y. Li, L. Zhang, Y.M. Xue, Z.Q. Zhou, Q. He, Chin. Phys. Lett. 23 (2006) 2259.

[8] A. Jager-Waldau, Sol. Energ. Mat. Sol. C. 95 (2011) 1509.

[9] T. Dalibor, S. Jost, H. Vogt, R. Brenning, A. Heiß, S. Visbeck, T. Happ, J. Palm, A. Avellán, T. Niesen, F. Karg, in: G. F. De Santi (Ed.), Advanced CIGSSe device for module efficiencies above 15%, Valencia, Spain, September 6-10, 2010, Proceedings of the 25th European Photovoltaic Solar Energy Conference and Exhibition / 5th World Conference on Photovoltaic Energy Conversion (2010) 2854.

[10] Z. Said-Bacar, Y. Leroy, F. Antoni, A. Slaoui, E. Fogarassy, Appl. Surf. Sci. 257, (2011) 5127.

[11] S. G. Ryu, I. Gruber, C. P. Grigoropoulos, D. Poulikakos, S. J. Moon, Thin Solid Films 520, (2012) 6724.

[12] D. Sands, J. E. Nicholls, J. H. C. Hogg, S. Chalk, F. X, Wagner, W. E. Hagstona, M. O'Neill, B. Lunn, D.E. Ashenford, J. Cryst. Growth 184/185, (1998) 114 .

[13] W. Tang, Z. Chen, S. He and H. Zhang, Procedia Chem. 1, (2009) 786.

[14] L. Schade, S. Franzka, S. Hardt, H. Wiggers, N. Hartmann, Appl. Surf. Sci. 278, (2013) 336.
[15] M. G. Kang, K. H. Cho, S. M. Oh, Y. H. Do, C. Y. Kang, S. Kim, S. J. Yoon, Curr. Appl. Phys. 11, (2011) 66.
[16] H.A. Al-Thani, F.S. Hasoon, M. Young, S. Asher, J.L. Alleman, M.M. Al-Jassim, D.L. Williamson, in: Proceedings of the 29th IEEE Photovoltaic specialists Conference (2002) 720.
[17] D. Rudmann, A.F. da Cunha, M. Kaelin, F. Kurdesau, H. Zogg, A.N. Tiwari, G. Bilger, Appl. Phys. Lett. 84 (2004) 1129.
[18] B. Tell, P.M. Bridenbaugh, J. Appl. Phys. 48, (1977) 2477.
[19] D. Liao, A. Rockett, Mat. Res. Soc. Symp. Proc. (2003) 763.
[20] K. Rammanathan, H. Wiesner, S. Asher, D. Niels, R.N. Bhattacharya, J. Keane, M.A. Contreras, R. Noufi, in: Proceedings of the 2nd World Conference Photovoltaic Solar Energy Conversion (1998) 477.
[21] Contreras, M.A., Tuttle, J,Gabor, A.Tennant, A.Ramanathan, K.Asher, S.Franz, A.Keane, J.Wang, L.Scofield, J. Noufi, R., *1st WCPEC.* (1994) *68.*
[22] L. Stolt, J. Hedstrom, J. Skarp, *1st WCPEC.* (1994) 250.
[23] D. Rudmann, Ph. D. thesis, University of Basel (2004).
[24] Optik & Photonik, 8, (2013) 4.
[25] Y. Taur, C.H. Wann, D.J. Frank, Int. Electron. Devices Meet. (1998) 789.
[26] E.C. Jones, E. Ishida, Mater. Sci. Eng. R24 (1998) 1.
[27] B. Yu, Y. Wang, H. Wang, Q. Xiang, C. Riccobene, S. Talwar, M. Lin, Tech. Dig. Int. Electron. Devices Meet. (1999) 509.
[28] Y. F. Chong, K. L. Pey, A. T. S. Wee, A. See, L. Chan, Y.F. Lu, W.D. Song, L.H. Chua, Appl. Phys. Lett. 76, (2000) 3197.
[29] S. Whelan, V. Privitera, M. Italia, G. Mannino, C. Bongiorno, C. Spinella, G. Fortunato, L. Mariucci, M. Stanizzi, A. Mittiga, J. Vac. Sci. Technol. B 20, (2002) 644.
[30] J. Herrero, C. Guill´en, Vacuum 67, (2002) 611.
[31] A. Kampmann, V. Sittinger, J. Rechid, R. Reineke-Koch, Thin Solid Films 361-362, (2000) 309.

[32] A. M. Hermann *et al.*, Sol. Energ. Mat. Sol. C. 70, (2001) 345.
[33] Y. C. Lin, J. H. Ke, W. T. Yen, S. C. Liang, C. H. Wu, C. T. Chiang, Appl. Surf. Sci. 257, (2011) 4278.
[34] S. T. Lakshmikumar and A. C. Rastogi, Appl. Phys. Lett. 66, (1995) 3128.
[35] A. Han, Y. Zhang, W. Song, B. Li, W. Liu, Y. Sun, Semicond. Sci. Technol. 27, (2012) 035022.
[36] I. Repins, S. Glynn, J. Duenow, T. J. Coutts, W. K. Metzger M. A. Contreras, in Preprint of Society of Photographic Instrumentation Engineers (SPIE) 2009 Solar Energy + Technology Conference (San Diego, CA, USA, August 2-6, 2009), p. 1.
[37] R. Sathyamoorthy, Sa. K. Narayandass, D. Mangalaraj, Sol. Energ. Mat. Sol. C. 76, (2003) 339.
[38] N. H. Kim, K. D. Myung, G. B. Cho and W. S. Lee, J. Korean Phys. Soc. 60, (2012) 425.
[39] I. Repins, M. A. Contreras, B. Egaas, C. DeHart, J. Scharf, C. L. Perkins, B. To, R. Noufi, Prog. Photovoltaics. 16, (2008) 235.
[40] D. H. Cho, K. S. Lee, Y. D. Chung, J. H. Kim, S. J. Park, J. Kim, Appl. Phys. Lett. 101, (2012) 023901.
[41] N.H. Kim, S. Oh, W.S. Lee, J. Korean Phys. Soc. 61 (2012) 1177.
[42] M. Venkatachalam, M. D. Kannan, S. Jayakumar, R. Balasundaraprabhu, N. Muthukumarasamy, Thin Solid Films 516 (2008) 6848.
[43] M. G. Panthani, V. Akhavan, B. Goodfellow, J. P. Schmidtke, L. Dunn, A. Dodabalapur, P. F. Barbara, B. A. Korgel, J. Am. Chem. Soc. 11 (2008) 16770.
[44] S. H. Han, F. S. Hasoon, J. W. Pankow, A. M. Hermann, D. H. Levi, Appl. Phys. Lett. 87 (2005) 151904.
[45] L. Zhang, F. Liu, F. Li, Q. He, B. Li, C. Li, Sol. Energ. Mat. Sol. C. 99 (2012) 356.
[46] G. Voorwinden, R. Kniese, M. Powalla, Thin Solid Films 431-432 (2003) 538.
[47] T. Duguet, S. Kenzari, V. Demange, T. Belmonte, J.-M. Dubois, V.

Fournée, J. Mater. Res. 25 (2010) 764.

[48] Zhao-Hui Li, Eou-Sik Cho, Sang Jik Kwon, Mario Dagenais, ECS Trans. 41 (2011) 241.

[49] S. Theodoropoulou, D. Papadimitriou, K. Anestou, Ch. Cobet, N. Esser, Semicond. Sci. Technol. 24 (2009) 015014.

[50] F. Meng, T. Sun, R. Cui, Semicond. Sci. Technol. 15 (2000) 926.

[51] M. M. Islam, A. Yamada, T. Sakurai, S. Ishizuka, K.Matsubara, S. Niki, K. Akimoto, Adv. Optoelectron. 2011 (2011) 573094.

[52] Y. F. Tu, S. Y. Huang, J. P. Sang, X. W Zou, J. Alloy. Compd. 482 (2009) 382.

[53] J. H. Lee, H. Y. Lee, Y. K. Park, S. H. Shin, K. J. Park, Jpn. J. Appl. Phys. 37, (1998) 3357.

[54] A. Romeo, D. L. B¨atzner, H. Zogg, A. N. Tiwari, Thin Solid Films 361, 420 (2000) 420.

[55] S. R. Aid, S. Matsumoto, G. Fuse, S. Sakuragi, Phys. Status Solidi A 208, (2011) 2772.

[56] R. O. Bell, M. Toulemonde, P. Siffen, Appl. Phys. 19, (1979) 313.

[57] Z. Hameiri n, L.Mai, T.Puzzer, S.R.Wenham, Solar Energy Materials & Solar Cells. 95 (2011) 1085.

[58] D. Souria, J. Non-Cryst. Solids 355, (2009) 1597.

[59] J. M. González-Leal, Mater. Lett. 39, (1999) 232.

[60] N. H. Kim, J. E. Jeon, G. B. Cho, W. S. Lee, D. Y. Choi, Int. J. Mod. Phys. B 27, (2013) 1350030.

감사의 글

석사학위를 마무리하는 이 시점에서 변함없는 모습으로 항상 저에게 힘이 되어 주시는 모든 분들에게 진심으로 감사드립니다.

가장 먼저 지도교수님이신 이우선 교수님과 김남훈 교수님께 감사의 말씀을 드립니다. 2년 동안 부족한 저에게 학문적, 인성적으로 많은 가르침을 주셨고 졸업이라는 작은 결실을 맺을 수 있도록 해주셨습니다. 두 분께서 주신 가르침은 제 인생에 있어 큰 밑거름이 될 것 이라고 생각합니다. 그리고 논문심사를 맡아주신 조금배 교수님과 최효상 교수님을 비롯한 조선대학교 전기공학과의 여러 은사님들께 감사드립니다.

가족의 힘이 없었으면 제가 이 자리에 있을 수 없었을 것입니다. 아들을 위해 항상 사랑과 헌신으로 돌보아 주신 아버지, 어머니 그리고 하나뿐인 동생에게도 이 기회를 빌어 사랑한다고 전하고 싶습니다. 앞으로는 제가 더 가족들을 위해 헌신하고 더욱 사랑하도록 노력하겠습니다.

대학원 생활을 돌이켜 보면 물성실험실 선후배를 비롯한 많은 이들의 도움이 있었기에 이렇게 학위 논문을 마무리 할 수 있었다고 생각합니다. 먼저 고필주, 전영길, 박주선, 박찬일 박사님을 비롯한 임채현, 명국도 선배님께 감사드리고, 하나뿐인 동기 전지은, 후배 유명한, 조도연 에게도 고맙다고 전하고 싶습니다. 그 외에도 함께 고생한 태양광 발전 실험실의 장인혁, 이권을 포함한 전력 계통 및 기기실험실의 선후배들... 그들과 함께했던 시간 잊지 못할 것입니다.

졸업할 때까지 항상 마음으로 함께 고생해 준 여자친구에게 고맙고 사랑한다는 말을 전하고 싶습니다. 그 밖에도 항상 저를 위해 마음을 써주시고 응원해주신 많은 분들에게 감사드리며 여러분의 앞날에 희망과 축복만이 가득하길 바라면서 감사의 글을 줄입니다.

감사합니다.

2013년 12월

오 성 하 올림

저작물 이용 허락서

학 과	전기공학과	학 번	20117443	과 정	석사
성 명	한글 : 오 성 하 한문 : 吳 成 夏 영문 : Oh Seongha				
주 소	광주광역시 남구 백운동 사직스카이 101-605				
연락처	010-3855-0137	E-mail	nike0128@nate.com		
논문제목	한글 : 스퍼터링 및 후속 열처리 공정으로 제조한CIGS 박막 특성				
	영문 : Characteristics of CIGS Thin Films Fabricated by Using Post-Annealing Processes after Sputtering				

본인이 저작한 위의 저작물에 대하여 다음과 같은 조건 아래 - 조선대학교가 저작물을 이용할 수 있도록 허락하고 동의합니다.

- 다 음 -

1. 저작물의 DB구축 및 인터넷을 포함한 정보통신망에의 공개를 위한 저작물의 복제, 기억장치에의 저장, 전송 등을 허락함.
2. 위의 목적을 위하여 필요한 범위 내에서의 편집과 형식상의 변경을 허락함. 다만, 저작물의 내용변경은 금지함.
3. 배포·전송된 저작물의 영리적 목적을 위한 복제, 저장, 전송 등은 금지함.
4. 저작물에 대한 이용기간은 5년으로 하고, 기간종료 3개월 이내에 별도의 의사 표시가 없을 경우에는 저작물의 이용기간을 계속 연장함.
5. 해당 저작물의 저작권을 타인에게 양도하거나 출판을 허락을 하였을 경우에는 1개월 이내에 대학에 이를 통보함.
6. 조선대학교는 저작물 이용의 허락 이후 해당 저작물로 인하여 발생하는 타인에 의한 권리 침해에 대하여 일체의 법적 책임을 지지 않음.
7. 소속 대학의 협정기관에 저작물의 제공 및 인터넷 등 정보통신망을 이용한 저작물의 전송·출력을 허락함.

동의여부 : 동의(○) 반대( )

2014년 2월

저작자: 오 성 하 (인)

조선대학교 총장 귀하